POLITECNICO DI MILANO

Scuola di Ingegneria Industriale e dell'Informazione

Corso di Laurea Magistrale in Ingegneria Fisica

Broadband Coherent Raman Microscopy

Relatore:

Prof. Dario Polli

Correlatore:

Prof. Giulio Cerullo

Tesi di laurea di:

Gustavo Ciardi

matr. 821211

Anno Accademico 2013/2014

Contents

List of Figures

List of Tables

Abstract in lingua italiana

La Spettroscopia Raman coerente è una tecnica di indagine chimica, completamente non invasiva, basata sulla risposta vibrazionale dei legami atomici. Il suo grande successo e le sue potenzialità fanno sì che gli studi e le applicazioni correlate si sviluppino da più di cinquanta anni. Grazie alla sua selettività e specificità, le applicazioni sono molteplici, dall'ottica biomedica, passando per la fisica dello stato solido, per arrivare all'individuazione di farmaci. In questa tesi viene sviluppato un approccio diverso rispetto alla maggior parte di quelli presenti oggigiorno in letteratura. Infatti le tecniche più usate ad oggi sono le così dette "Raman a singolo colore" (ovvero l'investigazione di una sola vibrazione molecolare alla volta). Ciò che viene proposto qui invece è innovativo, nel senso che quello che viene investigato e rivelato è più di un modo vibrazionale alla volta aumentando quindi la quantità di informazioni presenti in una singola misura. Questo approccio è chiamato "Raman a banda larga" (Broadband Raman) reso possibile dal recente sviluppo delle sorgenti laser a femtosecondi. In questa tesi ho sviluppato due approcci diversi di spettroscopia Raman coerente: CARS ("Coherent anti-Stokes Raman scattering") e l'SRS ("Stimulated Raman scattering") nella versioni a banda larga. Dapprima saranno illustrati i principi fisici e i processi alla base di queste tecniche. Successivamente verranno descritte le modalità di progettazione dell'apparato sperimentale insieme alla discussione e interpretazione dei dati sperimentali per entrambe le configurazioni. Per quanto riguarda il CARS i risultati ottenuti sono ancora preliminari, ma comunque significativi, poichè l'implementazione sperimentale è ancora in via di sviluppo. Per l'SRS invece è stato dimostrato un approccio completamente nuovo, basato sulla

rivelazione nel dominio del tempo (*Fourier Transform detection*), tramite uno speciale tipo di interferometro progettato all'interno del Politecnico di Milano. I risultati sono molto promettenti per future possibili applicazioni nel campo della medicina (ad esempio per la distinzione tra tessuti sani e tessuti tumorali) e dell'ottica biomedica.

Abstract

Coherent Raman Spectroscopy is a successful chemical investigation technique, entirely non-invasive and label-free, based on the vibrational response of the molecular bonds. Related research and studies are going on since more than fifty years. Owing to its great selectivity and specificity, applications are several, including for example biomedical optics, solid state physics and drug recognition. In this work a different approach is developed a with respect to the ones present nowadays in literature. Indeed, the mostly used techniques are the so called "single-colour Raman" (i.e. the investigation of a single molecular vibration at time). What is proposed here is innovative, meaning that we are able to detect more than a single vibrational mode at a time, increasing the quantity of information provided by a single measurement. This approach is called "Broadband Raman", made possible by femtosecond laser sources thanks to the femtosecond laser sources. The two employed techniques are, namely, CARS("Coherent anti-Stokes Raman scattering") and SRS("Stimulated Raman scattering"). in their broadband version. Firstly all the physical principles and processes are explained. Afterwards I will describe the experimental apparatus, together with the discussion and interpretation of experimental data, are described for both the configurations. Regarding the CARS, the results obtained are still preliminary, but however significant, because the development of the experiment is in progress. Conversely for SRS it is demonstrated a radically novel approach, based on the detection on the time domain (*Fourier Transform* detection), through the use of a special type of interferometer, entirely developed at Politecnico di Milano. The results are promising for possible future application in the medical field

(e.g. distinguish healthy tissue from tumor tissue).

Introduction

Raman spectroscopy techniques are breaking ground in several fields of science thanks to their noninvasive, label-free chemical species recognition. This identification relies on the characteristic vibrational transitions of chemical bonds and symmetry of the molecules. This means that different chemical compounds have their own *"vibrational fingerprint"*. This kind of non-destructive spectroscopy approach is a powerful tool for a lot of application, in particular biomedical optics (i.e. imaging of biological tissue, tumor diagnostics, DNA detection, and microendoscopy) which requires the perfect preservation of specimens, in contrast with the usual addition of, for example, fluorescent markers that can interfere with their biological function.

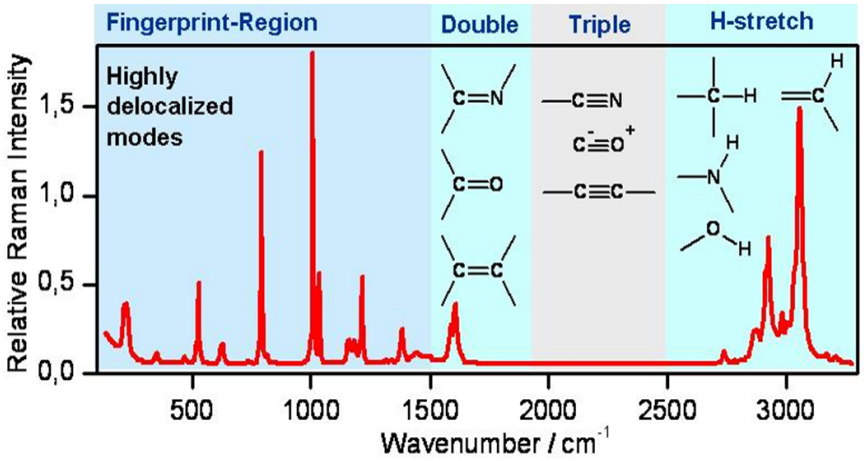

Figure 1: Example of vibrational fingerprint of a molecule in which are highlighted the regions of various chemical bonds

In other branches of physics, e.g. solid-state physics, spontaneous Raman spectroscopy is used to, among other things, characterize materials, measure temperature, and find the crystallographic orientation of a sample.

The ensemble of Raman techniques can be divided into two part: Spontaneous Raman Scattering and Coherent Raman Scattering. The primary disadvantage of spontaneous processes is the lack of speed. The scattering events from the illuminated samples are "random", meaning that only one photon among a trillion is Raman scattered and only less than 10% of these will be detected. This means that to collect enough photons (and hence achieve good contrast) long integration time are needed.

The alternative to spontaneous Raman scattering is a class of techniques collectively referred to as *coherent* Raman scattering(CRS). Instead of using a single light source, CRS uses two or more coherent synchronized laser sources(pump beam and Stokes beam) to excite the vibrational transitions. When the detuning of such sources matches the vibrational mode of the molecule, it is resonantly driven into oscillation. In CRS are included several techniques as **Coherent Anti-Stokes Raman Scattering(CARS)**, **Stimulated Raman Scattering(SRS)**, **Raman-induced Kerr-effect (RIKE)**. Due to the coherent nature of the involved optical process, extracted signals are order of magnitude higher than the ones obtained with spontaneous processes, yielding to more efficient and faster detection.

CARS has been recently the most popular from of CRS. It is a four wave interactions and has the great advantage of generating the resonant signal far away from the spectral regions of pump and Stokes, leading to a very simple detections free from beams resonant background. On the other hand, a significant distortion of the resonant signal is brought by the so called non-resonant background(NRB) (caused by interaction between the resonant and non-resonant part of the third order non-linear susceptibility of the specimen) and has a quadratic dependence on the molecule concentration of the sample, making difficult to detect less abundant species.

SRS is a two wave interaction and the generated Raman signal is linearly dependent on molecular concentration but sits on a resonant background given by the Stokes which is many orders of magnitude higher than the

Raman one (the ratio between the two is $\sim 10^{-4}$ or even less). The detection can be either performed on the pump [stimulated Raman loss(SRL)] or the Stokes [stimulated Raman Gain(SRG)].

RIKE slightly differs from CARS and SRS because it is based on the birefringence that occurs when the pump-Stokes frequency detuning is in resonance with a vibrational transition, leading to a polarization change on the Stokes(pump) field.

Usually these techniques are implemented with two narrow band laser pulses, where one of them(Stokes) is frequency tunable and sweeps an enough broad range of energies in such a way that the difference between the two can match more vibrational modes.

What i will show in this work are the results obtained with the "Broadband version" of SRS(BSRS) and CARS(BCARS) in which the Stokes beam is a ultra-broadband femtosecond pulse. Ideally in this way is possible to accede most of the Raman modes of the sample simultaneously, performing single shot measurements and hence to drastically reduce acquisition times.

In the first Chapter of this work all the mathematical instruments for the treatment of the topic will be given, together with an overview of techniques related to the Coherent Raman Scattering. Chapter 2 and 3 will be dedicated to BCARS and BSRS setup and the experimental data will be shown and discussed.

Chapter 1

Introduction to Coherent Raman Scattering processes

In this chapter I will introduce the mathematical foundations that lead to the complete description of the CRS processes, with a brief introduction on Spontaneous Raman Scattering, starting from the Maxwell's equations for electric and magnetic fields and reaching the four coupled equations for a medium with a third-order non-linearity. Afterwards I will explore the single-frequency interaction scheme for CARS, SRS and RIKE.

1.1 Spontaneous Raman Processes

As an electromagnetic wave (EM) interacts with matter, the electron orbits within the constituent molecules are perturbed periodically with the same frequency (ν_0) as the electric field of the incident wave. The oscillation or perturbation of the electron cloud results in a periodic separation of charge within the molecules, which is called an induced dipole moment. The oscillating induced dipole moment is manifest as a source of EM radiation, thereby resulting in scattered light. The majority of scattered light is emitted at the identical frequency (ν_0) of the incident light, a process referred to as elastic scattering also known as Rayleigh Scattering. However, as explained below, additional light is scattered at different frequencies, a process referred

to as inelastic scattering. Raman scattering is one such example of inelastic scattering. The induced dipole moment μ, is given by

$$\mu(t) = \alpha E(t) \tag{1.1}$$

where α is the polarizability and E is the the strength of electric field of the incident EM wave. The polarizability is a matter property that depends on the molecular structure and nature of the bonds. Let us study the effect of an incident EM wave on a molecule with a certain number of vibrational modes at frequency ν_{vib}. the molecule is at a fixed position in the sample, so that only the temporal profile of the EM wave is of interest and can be expressed as:

$$E(t) = E_0 \cos(2\pi\nu_0 t) \tag{1.2}$$

where ν_0 is the frequency of the incident e.m. wave ($\nu_0 = c/\lambda$). Substituting Eq 1.2 into Eq 1.1 yields the time-dependent induced dipole moment

$$\mu(t) = \alpha E_0 \cos(2\pi\nu_0 t) \tag{1.3}$$

Because the ability to perturb the local electron cloud of a molecular structure depends on the relative location of the individual atoms, it follows that the polarizability is a function of the instantaneous position of constituent atoms. The physical displacement dQ of the atoms about their equilibrium position, due to the particular vibrational mode, may be expressed as

$$dQ = Q_0 \cos(2\pi\nu_{vib} t) \tag{1.4}$$

where Q_0 is the maximum displacement about the equilibrium position. for example, for a typical diatomic molecule (e.g. N_2), the maximum displacement is about 10% of the bond length. For such small displacements, the polarizability may be approximated by a Taylor series expansion, namely,

$$\alpha = \alpha_0 + \frac{\partial \alpha}{\partial Q} dQ \tag{1.5}$$

where α_0 is the polarizability of the molecular mode at equilibrium position. Based on the vibrational displacement of Eq. 1.4 the polarizability may be given as

$$\alpha = \alpha_0 + \frac{\partial \alpha}{\partial Q} Q_0 \cos(2\pi \nu_{vib} t) \tag{1.6}$$

Finally Eq. 1.6 may be substituted into Eq. 1.3 which yields

$$\mu(t) = \alpha E_0 \cos(2\pi \nu_0 t) + \frac{\partial \alpha}{\partial Q} Q_0 E_0 \cos(2\pi \nu_{vib} t) \cos(2\pi \nu_0 t) \tag{1.7}$$

Using a trigonometric identity, the above relation may be rewritten as

$$\mu(t) = \alpha E_0 \cos(2\pi \nu_0 t) + \frac{\partial \alpha}{\partial Q} \frac{E_0 Q_0}{2} \{\cos[2\pi(\nu_0 - \nu_{vib})t] + \cos[2\pi(\nu_0 + \nu_{vib})t]\} \tag{1.8}$$

Examination of the above equation reveals that induced dipole moments are created at three distinct frequencies, namely ν_0, $[\nu_0 - \nu_{vib}]$ and $[\nu_0 + \nu_{vib}]$ which results in scattered radiation at these same three frequencies. The first scattered frequency corresponds to the incident frequency, hence is elastic scattering (i.e. Rayleigh Scattering), while the latter two frequencies are shifted to lower or higher frequencies and are therefore inelastic processes. The scattered light in these latter two cases is referred to as Raman scattering, with the down-shifted frequency (longer wavelength) referred to as Stokes scattering, and the up-shifted frequency (shorter wavelength) referred to as anti-Stokes scattering. C.V. Raman was the first to describe this type of inelastic scattering, for which he was awarded the Noble prize in physics in 1930.

1.2 Pulse propagation theory and description

Let us now develop the calculations in order to describe the Coherent Raman processes. The starting point are the Maxwell's equations:

$$\nabla \cdot \mathbf{D} = \rho \tag{1.9a}$$

$$\nabla \cdot \mathbf{B} = 0 \tag{1.9b}$$

$$\nabla \times \mathbf{E} = -\frac{\partial \mathbf{B}}{\partial t} \tag{1.9c}$$

$$\nabla \times \mathbf{B} = \mu_0(\mathbf{J} + \frac{\partial \mathbf{D}}{\partial t}) \tag{1.9d}$$

with the constitutive relations

$$\mathbf{D} = \varepsilon_0 \mathbf{E} + \mathbf{P} \tag{1.10a}$$

$$\mathbf{B} = \mu_0 \mathbf{H} + \mathbf{M} \tag{1.10b}$$

where $\mathbf{P}$ and $\mathbf{M}$ are respectively the polarization vector and the magnetization vector. In the following we will consider only media with negligible magnetization($\mathbf{M} \cong 0$), no free charges ($\rho = 0$) and currents($\mathbf{J} = 0$). In this way the previous equations simplify to:

$$\nabla \cdot \mathbf{D} = 0 \tag{1.11a}$$

$$\nabla \cdot \mathbf{B} = 0 \tag{1.11b}$$

$$\nabla \times \mathbf{E} = -\frac{\partial \mathbf{B}}{\partial t} \tag{1.11c}$$

$$\nabla \times \mathbf{B} = \mu_0 \varepsilon_0 \frac{\partial \mathbf{E}}{\partial t} + \mu_0 \frac{\partial \mathbf{P}}{\partial t} \tag{1.11d}$$

Applying the curl of both sides of (1.11c) we obtain:

$$\nabla \times \nabla \times \mathbf{E} = -\mu_0 \varepsilon_0 \frac{\partial^2 \mathbf{E}}{\partial t^2} - \mu_0 \frac{\partial^2 \mathbf{P}}{\partial t^2} \tag{1.12}$$

Recalling that $\nabla \times \nabla \times A = \nabla\nabla \cdot A - \nabla^2 A$ we obtain the wave equation(in our case we have$\nabla \cdot \mathbf{E} = 0$):

$$\nabla^2 \mathbf{E} = +\mu_0 \varepsilon_0 \frac{\partial^2 \mathbf{E}}{\partial t^2} + \mu_0 \frac{\partial^2 \mathbf{P}}{\partial t^2} \tag{1.13}$$

The Eq. 1.13 is a vector equation. First we make the **scalar approximation** by considering a linearly polarized pulse(orthogonal to the propagation direction) propagating in the z direction and considering only one component of the electric field vector:

$$\frac{\partial^2 E}{\partial z^2} + \nabla_T^2 E = +\mu_0 \varepsilon_0 \frac{\partial^2 E}{\partial t^2} + \mu_0 \frac{\partial^2 P}{\partial t^2}$$

where $\nabla_T^2 E = \frac{\partial^2 E}{\partial x^2} + \frac{\partial^2 E}{\partial y^2}$ is the so called *transverse Laplacian* operator. We further make the **plane wave approximation** by neglecting any transverse variation of the electric field:

$$\frac{\partial^2 E}{\partial z^2} - \frac{1}{c^2} \frac{\partial^2 E}{\partial t^2} = \mu_0 \frac{\partial^2 P}{\partial t^2} \tag{1.14}$$

where $c = 1/\sqrt{\mu_0 \varepsilon_0}$ is the speed of light in vacuum. Equation 1.14 already allows a first physical insight into the propagation of an electro-magnetic wave into a medium with polarization P. The polarization is on the right hand side of the equation, thus acts as a driving term for the electric field, modifying it during propagation.

Let us now consider a plane wave of the form:

$$E(z,t) = A(z,t) cos[\omega_0 t - k_0 z] \tag{1.15}$$

where A_1 is the field envelope (a real function), ω_0 is the carrier frequency and $k_0 = \frac{\omega_0}{c(\omega_0)} = \frac{\omega_0 n(\omega_0)}{c_0}$ is the wave-number in vacuum. It is often more convenient to rewrite Eq. 1.15 as:

$$E(z,t) = \mathrm{Re}\left\{A(z,t) \exp\left[i\left(\omega_0 t - k_0 z\right)\right]\right\} \tag{1.16}$$

where $A(z,t)$ is the complex field envelope. In the following we will avoid the expression $\mathrm{Re}\{...\}$ and write the electric field as:

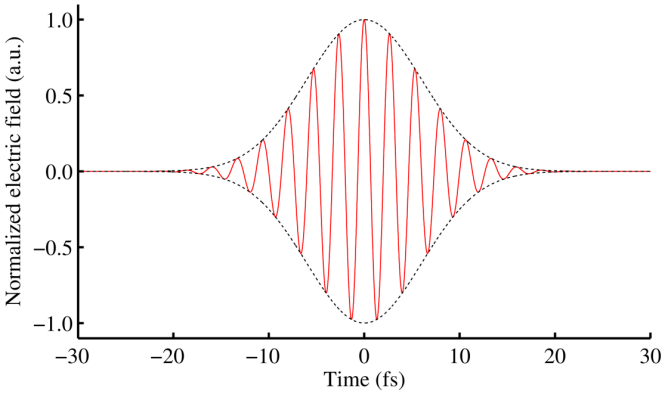

Figure 1.1: The real component of the electric field representing a Gaussian pulse with $10fs$ duration at $\lambda_0 = 0.8\mu m$. The dashed line represents the envelope function that is modulated by the underlying carrier wave, shown in red.

$$E(z,t) = A(z,t)\exp\left[i\left(\omega_0 t - k_0 z\right)\right] \tag{1.17}$$

It is however important to remember that the electric field is always a real quantity. Note that an alternative expression for Eq. 1.16 is:

$$\begin{aligned} E(z,t) =& \frac{1}{2}\left\{A(z,t)\exp\left[i\left(\omega_0 t - k_0 z\right)\right] + A^*(z,t)\exp\left[-i\left(\omega_0 t - k_0 z\right)\right]\right\} = \\ & \frac{1}{2}\left\{A(z,t)\exp\left[i\left(\omega_0 t - k_0 z\right)\right] + c.c.\right\} \end{aligned} \tag{1.18}$$

Similarly, the polarization can be written as [2]:

$$P(z,t) = p(z,t)\exp\left[i\left(\omega_0 t - k_p z\right)\right] \tag{1.19}$$

where we have assumed for generality that the wave-vector of the polarization k_p is different from that of the field k_0. The polarization is a function of the incident electric field and can be decomposed in the sum of a linear (P_L) and a non-linear (P_{NL}) component:

$$P(z,t) = P_L(z,t) + P_{NL}(z,t) \tag{1.20}$$

For the remainder of this section we will consider only the linear component (which k vector is the same of the electric field):

$$P(z,t) = P_L(z,t) = p_L(z,t)\left[i\left(\omega_0 t - k_0 z\right)\right] \tag{1.21}$$

and solve the equation:

$$\frac{\partial^2 E}{\partial z^2} - \frac{1}{c_0^2}\frac{\partial^2 E}{\partial t^2} = \mu_0 \frac{\partial^2 P_L}{\partial t^2} \tag{1.22}$$

Eq. 1.22 is more easily solved in the frequency domain, by introducing the Fourier transform:

$$\tilde{E}(z,\omega) = \mathcal{F}\left[E(z,t)\right] = \int_{-\infty}^{+\infty} E(z,t)\exp\left(-i\omega t\right) dt \tag{1.23}$$

It can be shown that the Fourier transform of E and P_L are [2]:

$$\tilde{E}(z,\omega) = \tilde{A}(z,\omega-\omega_0)\exp\left(-ik_0 z\right) \tag{1.24}$$

$$\tilde{P_L}(z,\omega) = \tilde{p_L}(z,\omega-\omega_0)\exp\left(-ik_0 z\right) \tag{1.25}$$

where $\tilde{A}(z,\omega) = \mathcal{F}\left[A(z,t)\right]$. By taking the Fourier transform of Eq. 1.22 and recalling the derivative rule for the Fourier transform [2]:

$$\mathcal{F}\left[\frac{d^n F(t)}{dt^n}\right] = (i\omega)^n \tilde{F}(\omega) \tag{1.26}$$

we obtain:

$$\frac{\partial^2 \tilde{E}}{\partial z^2} + \frac{\omega^2}{c_0^2}\tilde{E} = -\mu_0 \omega^2 \tilde{P_L} \tag{1.27}$$

It is possible to express the derivatives with respect to the longitudinal propagation coordinate z as follows:

$$\frac{\partial \tilde{E}}{\partial z} = \left(\frac{\partial \tilde{A}}{\partial z} - ik_0 \tilde{A} \right) \exp\left(-ik_0 z\right) \tag{1.28}$$

$$\frac{\partial^2 \tilde{E}}{\partial z^2} = \left(\frac{\partial^2 \tilde{A}}{\partial z^2} - 2ik_0 \frac{\partial \tilde{A}}{\partial z} - k_0^2 \tilde{A} \right) \exp\left(-ik_0 z\right) \tag{1.29}$$

By plugging Eq. 1.29 into Eq. 1.27 we obtain:

$$\frac{\partial^2 \tilde{A}}{\partial z^2} - 2ik_0 \frac{\partial \tilde{A}}{\partial z} - k_0^2 \tilde{A} + \frac{\omega^2}{c_0^2} \tilde{A} = -\mu_0 \omega^2 \tilde{p_L} \tag{1.30}$$

We use now the **Slowly Varying Envelope Approximation (SVEA)** [2], which consists in assuming that $\frac{\partial^2 \tilde{A}}{\partial z^2} << k_0 \frac{\partial \tilde{A}}{\partial z}$,corresponding to neglect variations of the envelope over propagation lengths of the order of the wavelength and breaks down only for extreme focusing (down to the diffraction limit). With this assumption it can be written that:

$$-2ik_0 \frac{\partial \tilde{A}}{\partial z} - k_0^2 \tilde{A} + \frac{\omega^2}{c_0^2} \tilde{A} = -\mu_0 \omega^2 \tilde{p_L} \tag{1.31}$$

To continue, an expression of $\tilde{p_L}(\omega)$ is needed. When light propagates through a material the electrons and atoms within it react to the electromagnetic fields of the wave, producing a change in the spatial and temporal distribution of electrical charges. The field causes small displacements of the valance electrons from their normal orbits, perturbations which create electric dipoles that are manifested as the electric polarization of the medium. For small field strengths (such as an unfocused, low energy laser beam) this electric polarization $\tilde{P}(\omega)$ is proportional to the electric field strength $\tilde{E}(\omega)$, expressed as:

$$\tilde{P_L}(\omega) = \epsilon_0 \chi^{(1)}(\omega) \tilde{E}(\omega) \tag{1.32}$$

where $\chi^{(1)}(\omega)$ is the linear (first-order) dielectric susceptibility. The definition of linear refractive index is $n_L(\omega) = \sqrt{\left(1 + \chi^{(1)}(\omega)\right)}$, then we obtain:

$$\tilde{p_L}(\omega) = \epsilon_0 \left[n_L^2(\omega) - 1 \right] \tilde{A}(\omega) \tag{1.33}$$

We finally obtain:

$$-2ik_0\frac{\partial\tilde{A}}{\partial z}-k_0^2\tilde{A}+\frac{\omega^2}{c_0^2}\tilde{A}=-\mu_0\epsilon_0\omega^2\left[n_L^2(\omega)-1\right]\tilde{A}=-\frac{\omega^2}{c_0^2}\left[n_L^2(\omega)-1\right]\tilde{A} \tag{1.34}$$

which simplifies to:

$$2ik_0\frac{\partial\tilde{A}}{\partial z}=\left[k^2\left(\omega\right)-k_0^2\right]\tilde{A} \tag{1.35}$$

with $k(\omega)=\frac{\omega}{c_0}n(\omega)$. In a dispersive medium, the refractive index is a function of frequency, and the wave-vector thus becomes a nonlinear function of ω. It is possible to write that [2]:

$$k^2\left(\omega\right)-k_0^2=\left[k\left(\omega\right)-k_0\right]\left[k\left(\omega\right)+k_0\right]\cong 2k_0\left[k\left(\omega\right)-k_0\right] \tag{1.36}$$

where the second equality is justified by the fact that the displacement between k_0 and $k(\omega)$ is little (i.e. $k(\omega)-k_0\ll k_0$). By a Taylor expansion of $k(\omega)$ around ω_0:

$$\begin{aligned}k(\omega)=&k_0+\left(\frac{dk}{d\omega}\right)_{\omega_0}(\omega-\omega_0)+\frac{1}{2}\left(\frac{d^2k}{d\omega^2}\right)_{\omega_0}(\omega-\omega_0)^2+\\&+\frac{1}{6}\left(\frac{d^3k}{d\omega^3}\right)_{\omega_0}(\omega-\omega_0)^3+...\end{aligned} \tag{1.37}$$

Usually an expansion up to the third order (or to the second order for moderate pulse bandwidths) is sufficient. By substituting Eq. 1.36 and Eq. 1.37 into Eq. 1.35, we obtain:

$$i\frac{\partial\tilde{A}\left(\omega-\omega_0\right)}{\partial z}\cong k_0'\left(\omega-\omega_0\right)\tilde{A}+\frac{1}{2}k_0''\left(\omega-\omega_0\right)^2\tilde{A}+\frac{1}{6}k_0'''\left(\omega-\omega_0\right)^3\tilde{A} \tag{1.38}$$

where $k_0'=\left(\frac{dk}{d\omega}\right)_{\omega_0}=\frac{1}{v_{g0}}$, v_{g0} is the group velocity of the carrier frequency;

$k_0'' = \left(\frac{d^2k}{d\omega^2}\right)_{\omega_0} = GVD$ is known as **Group Velocity Dispersion (GVD)** and $k_0''' = \left(\frac{d^3k}{d\omega^3}\right)_{\omega_0} = TOD$ is the **Third Order Dispersion (TOD)**. It is possible now to transform Eq. 1.38 back to the time domain. From Eq. 1.26 the following rule can be derived [2]:

$$\mathcal{F}^{-1}\left[\omega^n \tilde{F}(\omega)\right] = (-i)^n \frac{d^n F(t)}{dt^n} \tag{1.39}$$

Obtaining:

$$\frac{\partial A(z,t)}{\partial z} + \frac{1}{v_{g0}}\frac{\partial A}{\partial t} - \frac{i}{2}k_0''\frac{\partial^2 A}{\partial t^2} + \frac{1}{6}k_0'''\frac{\partial^3 A}{\partial t^3} = 0 \tag{1.40}$$

Eq. 1.40 can be simplified by changing to a temporal frame of reference moving with the group velocity of the carrier wave (like sitting on top of traveling pulse): $z' = z, \tau = t - \frac{z}{v_{g0}}$, obtaining:

$$\begin{aligned} &\frac{\partial}{\partial t} = \frac{\partial}{\partial z'}\frac{\partial z'}{\partial t} + \frac{\partial}{\partial \tau}\frac{\partial \tau}{\partial t} = \frac{\partial}{\partial \tau} \\ &\frac{\partial^n}{\partial t^n} = \frac{\partial^n}{\partial \tau^n} \\ &\frac{\partial}{\partial z} = \frac{\partial}{\partial z'}\frac{\partial z'}{\partial z} + \frac{\partial}{\partial \tau}\frac{\partial \tau}{\partial z} = \frac{\partial}{\partial z} - \frac{1}{v_{g0}}\frac{\partial}{\partial \tau} \end{aligned} \tag{1.41}$$

In this new frame of reference Eq. 1.40 becomes:

$$\frac{\partial A}{\partial z'} - \frac{i}{2}k_0''\frac{\partial^2 A}{\partial \tau^2} + \frac{1}{6}k_0'''\frac{\partial^3 A}{\partial \tau^3} = 0 \tag{1.42}$$

In the case, often satisfied in practice, in which one can assume $k_0''' \cong 0$, Eq. 1.42 further simplifies to:

$$\frac{\partial A}{\partial z'} - \frac{i}{2}k_0''\frac{\partial^2 A}{\partial \tau^2} = 0 \tag{1.43}$$

Eq. 1.43, also known as the parabolic equation, captures the main physics of linear propagation of ultrashort pulses in dispersive media. Let us study the propagation of a pulse, with a known envelope at $z = 0$, $A(0,t) = A_0(t)$.

Starting with the simplified case of a non-dispersive medium, in which the

refractive index is constant with frequency: $n(\omega) = n(\omega_0) = const$. In this case $k(\omega) = \frac{\omega}{c_0} n(\omega_0)$ is a linear function of frequency, and $k_0'' = 0$. We then have: $\frac{\partial A(z,\tau)}{\partial z} = 0$ which gives $A(L,\tau) = const = A_0(\tau) = A_0\left(t - \frac{L}{v_{g0}}\right)$. We thus have a pulse that moves with the group velocity of the carrier frequency (so that its peak position shifts linearly with time) but maintains its shape unaltered. Note that, strictly speaking, only the vacuum is a non-dispersive medium. The spectrum of the pulse after propagation acquires a linear phase:

$$\tilde{A}(L,\omega) = \tilde{A}(0,\omega) \exp\left(-i\frac{L}{v_{g0}}\omega\right) = \tilde{A}(0,\omega) \exp\left(-i\tau_{g0}\omega\right) \tag{1.44}$$

where $\tau_{g0} = \frac{L}{v_{g0}}$ is called the **group delay** of the carrier frequency, and is the delay of the pulse envelope upon propagation in a non-dispersive medium.

Turning now to a dispersive medium; Eq. 1.43 can be solved by taking a Fourier transform with respect to time:

$$\frac{\partial \tilde{A}(z,\omega)}{\partial z} + \frac{i}{2}\omega^2 k_0'' \tilde{A} = 0 \tag{1.45}$$

Eq. 1.45 can be easily solved by separation of variables:

$$\tilde{A}(L,\omega) = \tilde{A}(0,\omega) \exp\left(-\frac{i}{2} D_2 \omega^2\right) \tag{1.46}$$

where it has been defined $D_2 = k_0'' L$ as the **second order dispersion (or Group Delay Dispersion, GDD)** [2]. It should be noted that, since the phase shift induced by propagation through a length L can be expressed as $\phi(\omega) = k(\omega)L$, one can write $D_2 = \left(\frac{d^2\phi}{d\omega^2}\right)_{\omega_0}$. Now going back to the time domain:

$$A(L,t) = \frac{1}{2\pi} \int_{-\infty}^{+\infty} \tilde{A}(0,\omega) \exp\left(-\frac{i}{2} D_2 \omega^2\right) \exp(i\omega t)\, d\omega \tag{1.47}$$

Eq. 1.46 can be numerically solved for any input pulse; it is possible to see that the effect of propagation in a dispersive medium is to add to the

spectrum a **quadratic phase** [2]. An analytical solution of 1.47 is possible only in the special case of a Gaussian pulse shape:

$$A_0(\tau) = A_0 \exp\left(-\frac{\tau^2}{2\tau_p^2}\right) \tag{1.48}$$

This pulse shape, although it does not realistically represent many ultrashort laser pulses, is amenable to analytical calculation, because the Fourier transform of a Gaussian function is also Gaussian. The parameter τ_p defines the pulse duration; for an ultrashort pulse, in particular, one usually specifies the intensity Full Width at Half Maximum (FWHM), which is given by:

$$\tau_{FWHM} = \sqrt{2ln(2)}\tau_p \tag{1.49}$$

By recalling that:

$$\mathcal{F}\left[\exp\left(-at^2\right)\right] = \sqrt{\frac{\pi}{a}} \exp\left(-\frac{\omega^2}{4a}\right) \tag{1.50}$$

And putting $a = 1/2\tau_p^2$ we obtain:

$$\tilde{A}_0(\omega) = \sqrt{2\pi}\tau_p A_0 \exp\left(-\frac{\tau_p^2\omega^2}{2}\right) \tag{1.51}$$

and, after propagation:

$$\tilde{A}(L,\omega) = \sqrt{2\pi}\tau_p A_0 \exp\left[-\frac{\tau_p^2}{2}\omega^2\left(1 + i\frac{D_2}{\tau_p^2}\right)\right] \tag{1.52}$$

Transforming back to the time domain, we obtain:

$$\begin{aligned} A(L,\tau) =& \frac{A_0\tau_p}{\sqrt{\tau_p^2 + iD_2}} \exp\left[-\frac{\tau^2}{2\left(\tau_p^2 + iD_2\right)}\right] = \\ & \frac{A_0\tau_p}{\sqrt{\tau_p^2 + iD_2}} \exp\left(-\frac{\tau^2}{2\tau_{out}^2}\right) \exp\left[i\phi(\tau)\right] \end{aligned} \tag{1.53}$$

where:

$$\tau_{out}^2 = \tau_p^2 + \frac{D_2^2}{\tau_p^2} = \tau_p^2 \left[1 + \left(\frac{D_2}{\tau_p^2}\right)^2\right] \tag{1.54}$$

and:

$$\phi(\tau) = \frac{D_2 \tau^2}{2\left(\tau_p^4 + D_2^2\right)} \tag{1.55}$$

By recalling that $D_2 = k_0'' L$ and defining a "**dispersion length**" $L_D = \frac{\tau_p^2}{k_0''}$, Eq. 1.54 can be rewritten as:

$$\tau_{out} = \tau_p \sqrt{1 + \left(\frac{L}{L_D}\right)^2} \tag{1.56}$$

Eq. 1.56 already allows a physical insight into the mechanism of dispersive pulse broadening. For short propagation lengths, $L << L_D$, the pulse-width remains basically unchanged upon propagation, while for long propagation, $L >> L_D$, a linear broadening with distance appears, $\tau_{out} = \frac{\tau_p}{L_D} L$.

Note that the temporal spreading of the Gaussian pulse due to dispersion has the same expression as the spatial spreading of a Gaussian beam due to diffraction [2]:

$$w(z) = w_0 \sqrt{1 + \left(\frac{z}{z_R}\right)^2} \tag{1.57}$$

where the Rayleigh range, defined as $z_R = \frac{n\pi w_0^2}{\lambda}$, plays a similar role to the dispersion length L_D.

Let's now consider the time-dependent temporal phase. By recalling that the ultrashort pulse is written as:

$$E(z,\tau) = |A(z,\tau)| \exp\left[i\left(\omega_0 \tau - k_0 z + \phi(\tau)\right)\right] \tag{1.58}$$

The instantaneous pulse frequency becomes:

$$\omega_i(\tau) = \omega_0 + \frac{d\phi}{d\tau} = \omega_0 + \frac{2D_2}{2\left(\tau_p^4 + D_2^2\right)} \tag{1.59}$$

The frequency is thus not constant, but displays a linear temporal variation, or "**chirp**". In particular, for $D_2 > 0$, the frequency increases with time ("positive chirp" or "up-chirp"), while for $D_2 < 0$, the frequency decreases with time ("negative chirp" or "down-chirp").

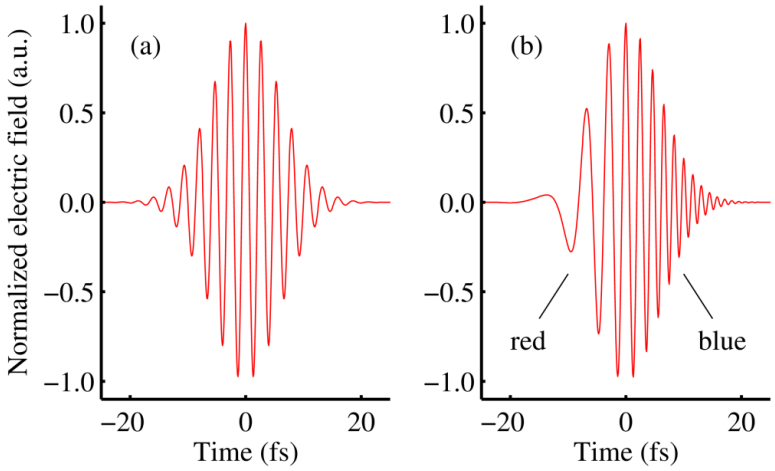

Figure 1.2: A $10fs$ pulse (a) before and (b) after positive dispersive broadening. Higher blue frequencies are delayed relative to the lower red frequencies.

To understand this behaviour, let's recall that: $D_2 \propto \frac{d}{d\omega}\frac{dk}{d\omega} = \frac{d}{d\omega}\left(\frac{1}{v_g(\omega)}\right)$ so that $D_2 > 0$ means that v_g decreases with frequency (and viceversa for $D_2 < 0$). For $D_2 > 0$, therefore, the higher frequencies (blue components of the spectrum) will move at lower speed with respect to the lower frequencies (red components of the spectrum) and get delayed. The pulse thus acquires an up-chirp. The opposite holds for the case of a down-chirp.

To further understand this point, let's express the laser pulse like an inverse Fourier transform [2]:

$$E(t) = \frac{1}{2\pi}\int_{-\infty}^{+\infty} \left|\tilde{E}(\omega)\right| \exp\left[-i\phi(\omega)\right] \exp(i\omega t)\, d\omega \tag{1.60}$$

Let us now slice from the pulse spectrum a narrow interval of frequencies around a given frequency $\bar{\omega}$:

$$E_{\bar{\omega}}(t) = \frac{1}{2\pi}\int_{\bar{\omega}-\Delta\omega}^{\bar{\omega}+\Delta\omega} \left|\tilde{E}(\omega)\right| \exp\left[-i\phi(\omega)\right] \exp(i\omega t)\, d\omega \tag{1.61}$$

By expanding $\phi(\omega)$ around $\bar{\omega}$ it is possible to write that:

$$\begin{aligned} E_{\bar{\omega}}(t) =& \frac{1}{2\pi} e^{(-i\bar{\omega}t)} \int_{\bar{\omega}-\Delta\omega}^{\bar{\omega}+\Delta\omega} \left|\tilde{E}(\omega)\right| e^{\left[-i\phi(\bar{\omega})-i\left(\frac{d\phi}{d\omega}\right)_{\bar{\omega}}(\omega-\bar{\omega})\right]} e^{[i(\omega-\bar{\omega})t]} d\omega = \\ &= \frac{1}{2\pi} e^{[i(\bar{\omega}t-\phi(\bar{\omega}))]} \int_{\bar{\omega}-\Delta\omega}^{\bar{\omega}+\Delta\omega} \left|\tilde{E}(\omega)\right| e^{\left[i(\omega-\bar{\omega})\left(t-\left(\frac{d\phi}{d\omega}\right)_{\bar{\omega}}\right)\right]} d\omega \end{aligned} \tag{1.62}$$

One can easily see that the right hand side of the equation is non-vanishing only when the argument of the exponential is zero, i.e. when:

$$t = \tau_g(\bar{\omega}) = \left(\frac{d\phi}{d\omega}\right)_{\bar{\omega}}$$

The **group delay** τ_g is thus the relative arrival time of a given frequency wave-packet within the pulse. By a Taylor expansion of the spectral phase:

$$\begin{aligned} \phi(\omega) =& \phi(\omega_0) + \left(\frac{d\phi}{d\omega}\right)_{\omega_0}(\omega-\omega_0) + \frac{1}{2}\left(\frac{d^2\phi}{d\omega^2}\right)_{\omega_0}(\omega-\omega_0)^2 + \\ &+ \frac{1}{6}\left(\frac{d^3\phi}{d\omega^3}\right)_{\omega_0}(\omega-\omega_0)^3 + ... = \\ &= \phi(\omega_0) + \tau_{g0}(\omega-\omega_0) + \frac{1}{2}D_2(\omega-\omega_0)^2 + \frac{1}{6}D_3(\omega-\omega_0)^3 + ... \end{aligned} \tag{1.63}$$

where $D_3 = \left(\frac{d^3\phi}{d\omega^3}\right)_{\omega_0}$ is called **third-order dispersion (TOD)**. One can thus write:

$$\tau_g(\omega) = \frac{d\phi(\omega)}{d\omega} = \tau_{g0} + D_2(\omega-\omega_0) + \frac{1}{2}D_3(\omega-\omega_0)^2 + ... \tag{1.64}$$

Eq. 1.64 shows that for $D_2 = D_3 = 0$ all the frequency components of the

pulse arrive simultaneously, so that it is called Transform-Limited (TL), while in all other cases the different frequency components arrive at different times and the pulse becomes chirped. In particular, if the D_2 term is dominant (quadratic chirp) then the group delay varies linearly with frequency, meaning that the instantaneous frequency is swept within the pulse envelope (from red to blue for positive chirp and from blue to red for negative chirp).

1.3 Elements of Non-Linear Optics

In previous sections the description was limited in the particular case where only the linear polarization was present. Let us now consider also the terms involving the non-linear polarization. In this work we will focus on the third order non-linear optics, the most significant process involved in the Raman transition behavior. Starting with the equation:

$$\frac{\partial^2 E}{\partial z^2} - \frac{1}{c_0^2}\frac{\partial^2 E}{\partial t^2} = \mu_0 \frac{\partial^2 P_L}{\partial t^2} + \mu_0 \frac{\partial^2 P_{NL}}{\partial t^2} \tag{1.65}$$

where:

$$P_{NL}(z,t) = p_{NL}(z,t) \exp\left[i\left(\omega_0 t - k_p z\right)\right] \tag{1.66}$$

having emphasized that the wave-number k_p of the nonlinear polarization at ω_0(with respect to the case of linear polarization) is different from that of the electric field. The second derivative of the nonlinear polarization can be expressed as:

$$\frac{\partial^2 P_{NL}}{\partial t^2} = \left(\frac{\partial^2 p_{NL}}{\partial t^2} + 2i\omega_0 \frac{\partial p_{NL}}{\partial t} - \omega_0^2 p_{NL}\right) \exp\left[i\left(\omega_0 t - k_p z\right)\right] \tag{1.67}$$

Now making the approximation that the envelope p_{NL} varies slowly over the timescale of an optical cycle [2], so that:

$$\frac{\partial^2 p_{NL}}{\partial t^2}, \omega_0 \frac{\partial p_{NL}}{\partial t} << \omega_0^2 p_{NL} \tag{1.68}$$

Equation 1.67 then becomes:

$$\frac{\partial^2 P_{NL}}{\partial t^2} \cong -\omega_0^2 p_{NL} \exp\left[i\left(\omega_0 t - k_p z\right)\right] \tag{1.69}$$

By plugging Eq. 1.69 into Eq. 1.65 and solving it in the same way it was reported in the previous section, we obtain [2]:

$$-2ik_0\frac{\partial A}{\partial z} - 2\frac{ik_0}{v_{g0}}\frac{\partial A}{\partial t} - k_0 k_0''\frac{\partial^2 A}{\partial t^2} = -\mu_0\omega_0^2 p_{NL}\exp\left[-i\Delta k z\right] \tag{1.70}$$

where $\Delta k = k_p - k_0$ is the so-called "**wave-vector mismatch**" between the nonlinear polarization and the field. Eq. 1.70, recalling that $\omega_0/k_0 = c_0/n\left(\omega_0\right)$, can be rewritten as:

$$\frac{\partial A}{\partial z} + \frac{1}{v_{g0}}\frac{\partial A}{\partial t} - \frac{i}{2}k_0''\frac{\partial^2 A}{\partial t^2} = -i\frac{\mu_0\omega_0 c_0}{2n_0}p_{NL}\exp\left[-i\Delta k z\right] \tag{1.71}$$

1.3.1 Nonlinear susceptibility

As done for linear polarization (Eq.1.32) an expression for the non-linear polarization is needed. For intense electric fields, as the ones of ultrashort broadband pulses, a nonlinear polarization of the medium takes place, described as a power series expansion of Eq. 1.32 and often written as:

$$\tilde{P}\left(\omega\right) = \epsilon_0\left[\chi^{(1)}\tilde{E}\left(\omega\right) + \chi^{(2)}\tilde{E}^2\left(\omega\right) + \chi^{(3)}\tilde{E}^3\left(\omega\right) + ...\right] \tag{1.72}$$

where $\chi^{(2)}$ and $\chi^{(3)}$ are the second-order and third-order nonlinear susceptibilities respectively. Nonlinear optical interactions can be described in terms of a nonlinear polarization given by Eq 1.72 only for a material system that is lossless and dispersionless. In a more general case the nonlinear susceptibility becomes a complex quantity relating the complex amplitudes of the electric field and polarization. Here for simplicity we assume P and E to be scalar quantities. Considering the vector nature of the fields the $\chi^{(1)}$ becomes a

second-rank tensor, $\chi^{(2)}$ becomes a third-rank tensor, and so on. Some hints about tensor nature of nonlinear susceptibility will be given in Section 1.4.4.

It is worth noting that power series representation of the nonlinear optical response described by Eq. 1.72 is not rigorously correct because it assumes the response is instantaneous. However, the response is not infinitely fast. In the case of the bound-electronic nonlinearity for example, this assumption is excellent because the response is exceedingly fast. Response times can vary by orders of magnitude depending on the physical mechanism and resonance conditions involved. Furthermore, Eq. 1.72 assumes locality, which implies the nonlinear polarization at a given point in space depends on the magnitude of the electric field only at that point. This two conditions are not always satisfied, but we will consider them satisfied for our purpose. While all transparent materials display first- and third-order nonlinear susceptibility, second-order(and in general even orders) effects are only observed in non-centrosymmetric crystals [2]. Typical $\chi^{(2)}$ effects are Second Harmonic Generation (SHG), Sum Frequency Generation (SFG) and Difference frequency generation (DFG).

The third-order nonlinear susceptibility can be exploited to produce a number of nonlinear interactions. A formal derivation of these processes will be given in the next section; however a more general outline will be given first here. The most common application of the $\chi^{(3)}$ non-linearity is to facilitate frequency mixing between three electromagnetic waves to produce an interfering field E, given by:

$$E(z,t) = E_1(z,t) + E_2(z,t) + E_3(z,t) \tag{1.73a}$$

$$E(z,t) = \frac{1}{2}[A_1 e^{i(\omega_1 t - k_1 z)} + A_2 e^{i(\omega_2 t - k_2 z)} + A_3 e^{i(\omega_1 t - k_1 z)} + c.c.] \tag{1.73b}$$

The term involving E^3 in Eq. 1.72 implies that three optical fields interact to produce a fourth field. The $\chi^{(3)}$ interaction is thus a four-field process and conservation of photon energy is always required to complete the interaction process. It is important to realize that there can be up to three different

input laser frequencies, but there can be as few as one. Ignoring the $\chi^{(1)}$ and $\chi^{(2)}$ components in Eq. 1.72 the nonlinear polarization resulting from the E^3 interactions leads to a total of 108 terms involving all possible permutations of the fields at three frequencies. The non linear polarization occurs at the frequency given by:

$$\omega_4 = \pm\omega_i \pm \omega_j \pm \omega_k \qquad \text{for} \quad i, j, k = 1, 2, 3 \tag{1.74}$$

The existence of 108 terms does not mean there are as many distinct mechanisms involved. For instance, three terms give $\omega_4 = 3\omega_j$, for $j = 1, 2, 3$, describing exactly the same process, third harmonic generation (THG). Propagation of interacting beams is also an important consideration and one must account for wavevector summation (i.e. conservation of momentum) that results from the E^3 operation. This requirements implies that only the processes which satisfy

$$k_4 = \pm k_i \pm k_j \pm k_k \qquad \text{for} \quad i, j, k = 1, 2, 3 \tag{1.75}$$

are effectively efficient. This condition is known as **phase matching condition**.

1.3.2 Third Order Non-Linear Optics

Four-Wave Mixing

Let's consider the superposition of four fields, at frequencies ω_1, ω_2, ω_3 and ω_4:

$$E(z,t) = \sum_{n=1}^{4} A_n(z,t) \exp[i(\omega_n t - k_n z)] \tag{1.76}$$

with:

$$\omega_1 + \omega_3 = \omega_4 + \omega_2 \tag{1.77}$$

impinging on a medium with a third-order nonlinear response:

$$P_{NL}(z,t) = \epsilon_0 \chi^{(3)} E^3(z,t) \tag{1.78}$$

Such a situation corresponds to an exchange of energy between the four fields by means of the third-order non-linearity. The nonlinear polarization will contain four components at frequencies ω_1, ω_2 and ω_3 given by [2]:

$$\begin{aligned}
P^1_{NL}(z,t) &= \frac{3\epsilon_0\chi^{(3)}}{2} A_2 A_3^* A_4 \exp\left\{i\left[(\omega_2 - \omega_3 + \omega_4)t - (k_2 - k_3 + k_4)z\right]\right\} + c.c. \\
P^2_{NL}(z,t) &= \frac{3\epsilon_0\chi^{(3)}}{2} A_1 A_3 A_4^* \exp\left\{i\left[(\omega_1 + \omega_3 - \omega_4)t - (k_1 + k_3 - k_4)z\right]\right\} + c.c. \\
P^3_{NL}(z,t) &= \frac{3\epsilon_0\chi^{(3)}}{2} A_1^* A_2 A_4 \exp\left\{i\left[(\omega_2 - \omega_1 + \omega_4)t - (k_2 - k_1 + k_4)z\right]\right\} + c.c \\
P^4_{NL}(z,t) &= \frac{3\epsilon_0\chi^{(3)}}{2} A_1 A_2^* A_3 \exp\left\{i\left[(\omega_1 - \omega_2 + \omega_3)t - (k_1 - k_2 + k_3)z\right]\right\} + c.c
\end{aligned} \tag{1.79}$$

Obviously there are other terms on P_{NL} at different frequencies. Here we consider only the terms at ω_1, ω_2, ω_3 and ω_4 by assuming that only the interaction between these four fields is efficient, due to the phase-matching condition. It is possible then to derive from Eq. 1.71 the following four equations [2] for the fields at ω_1, ω_2, ω_3 and ω_4:

$$\frac{\partial A_1}{\partial z} + \frac{1}{v_{g1}}\frac{\partial A_1}{\partial t} - \frac{i}{2}k_1''\frac{\partial^2 A_1}{\partial t^2} = -i\alpha_1\chi^{(3)} A_2 A_3^* A_4 \exp[-i\Delta k z] \tag{1.80}$$

$$\frac{\partial A_2}{\partial z} + \frac{1}{v_{g2}}\frac{\partial A_2}{\partial t} - \frac{i}{2}k_1''\frac{\partial^2 A_2}{\partial t^2} = -i\alpha_2\chi^{(3)} A_1 A_3 A_4^* \exp[-i\Delta k z] \tag{1.81}$$

$$\frac{\partial A_3}{\partial z} + \frac{1}{v_{g3}}\frac{\partial A_3}{\partial t} - \frac{i}{2}k_1''\frac{\partial^2 A_3}{\partial t^2} = -i\alpha_3\chi^{(3)} A_1^* A_2 A_4 \exp[-i\Delta k z] \tag{1.82}$$

$$\frac{\partial A_4}{\partial z} + \frac{1}{v_{g4}}\frac{\partial A_4}{\partial t} - \frac{i}{2}k_1''\frac{\partial^2 A_4}{\partial t^2} = -i\alpha_4\chi^{(3)}A_1A_2^*A_3\exp[i\Delta kz] \tag{1.83}$$

with $\Delta k = k_2 - k_1 + k_4 - k_3$, and $\alpha_i = \frac{3\omega_i}{4cn_i}$. The four equations are coupled nonlinear partial differential equations, and in general not amenable to an analytic solution and must be treated numerically. A first simplification, that captures the main physics of parametric interaction, consists in neglecting the GVD terms, i.e. putting $k_i'' = 0$. This is justified by considering that the four interacting pulses are propagating at very different group velocities v_{gi} [2]. The effects of this group velocity difference are much more relevant than those of group velocity dispersion between the different frequency components of a single pulse. The second approximation we make is to consider quasi-monochromatic waves, that is $\frac{\partial}{\partial t} = 0$. With such simplifications the four coupled equations become:

$$\frac{dA_1}{dz} = -i\alpha_1\chi^{(3)}A_2A_3^*A_4\exp[-i\Delta kz] \tag{1.84a}$$
$$\frac{dA_2}{dz} = -i\alpha_2\chi^{(3)}A_1A_3A_4^*\exp[-i\Delta kz] \tag{1.84b}$$
$$\frac{dA_3}{dz} = -i\alpha_3\chi^{(3)}A_1^*A_2A_4\exp[-i\Delta kz] \tag{1.84c}$$
$$\frac{dA_4}{dz} = -i\alpha_4\chi^{(3)}A_1A_2^*A_3\exp[i\Delta kz] \tag{1.84d}$$

These equations will be the starting point to describe all the coherent Raman techniques.

1.4 Coherent Raman Scattering Microscopy(CRS)

As already outlined in the Introduction, CRS microscopy uses two synchronized train of laser pulses at frequency ω_p (Pump frequency) and ω_S (Stokes frequency) providing resonant excitation of Raman transition through

the third-order nonlinear optical response of the sample by setting up and detecting a **vibrational coherence** within the molecules in laser focus.

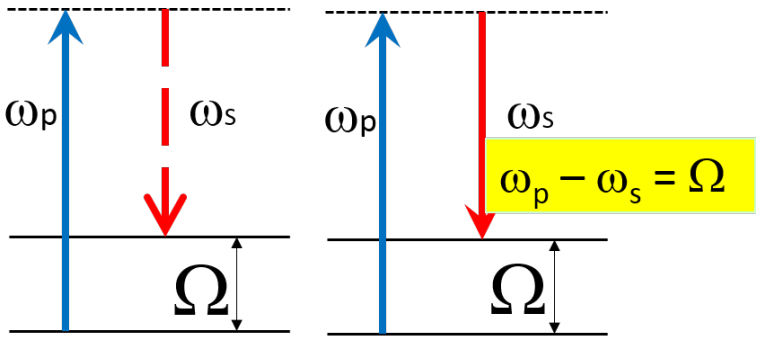

(a) (b)

Figure 1.3: Difference between Spontaneous Raman Scattering (a) and Coherent Raman Scattering(b). The dashed red line represents the inelastically scattered light that is energetically downshifted by the characteristic vibrational frequency of a molecule (Stokes light). Conversely continuous red line represents the coherently driven radiation (stimulated emission) emitted in presence of simultaneous pump and Stokes beam. The dashed black lines stand for virtual levels.

When the difference between pump and Stokes frequencies matches a characteristic vibrational frequency Ω (i.e. $\omega_p - \omega_S = \Omega$) all the molecules in the focal volume are made to **vibrate in phase**. This vibrational coherence enhances the Raman response by many orders of magnitude with respect to the incoherent spontaneous Raman process.

To better understand what we are able to extract from a Raman spectrum we need to focus on the information that third-order nonlinear susceptibility can provide. The $\chi^{(3)}$ consists of a resonant and non-resonant contribution [3]:

$$\chi^{(3)} = \chi^{(3)}_R(\Delta) + \chi^{(3)}_{NR}, \tag{1.85}$$

where

$$\chi_R^{(3)}(\Delta) \propto \frac{N}{\Delta - i\Gamma} \qquad \text{and} \qquad \chi_{NR}^{(3)} = const. \tag{1.86}$$

The $\chi_{NR}^{(3)}$ it is a purely real and constant function of ω; it accounts for all the other molecules present in the sample which are not the investigated ones and for nonlinear response of bound electrons to an applied optical field. The $\chi_R^{(3)}(\Delta)$ is a Lorentzian linewidth function(Fig 1.4) related to the molecules vibrating at the frequency we are interested in, where:

- $\Delta = \omega_p - \omega_S - \Omega$ is the **frequency detuning**
- Γ is the **homogenous width** of the Raman line
- N is the **density** of vibrational oscillators

The resonant third-order susceptibility can be further decomposed in the real and imaginary part:

$$\chi_R^{(3)}(\Delta) = \mathrm{Re}\{\chi_R^{(3)}(\Delta)\} + i\,\mathrm{Im}\{\chi_R^{(3)}(\Delta)\} \tag{1.87}$$

with

$$\mathrm{Re}\{\chi_R^{(3)}(\Delta)\} \propto \frac{N\Delta}{\Delta^2 + \Gamma^2} \qquad \text{and} \qquad \mathrm{Im}\{\chi_R^{(3)}(\Delta)\} \propto \frac{N\Gamma}{\Delta^2 + \Gamma^2} \tag{1.88}$$

The real and imaginary part of the $\chi_R^{(3)}$ have respectively a dispersive and Lorentzian lineshape as shown in Fig. 1.4 .

1.4.1 Stimulated Raman Scattering (SRS)

In SRS the coherent interaction with the sample and the consequent exchange of energy with input laser beams, induce stimulated emission from a virtual state to the investigated vibrational state, resulting in a Stokes field amplification and simultaneous pump beam attenuation. This situation is represented in Fig 1.3. For SRS the conditions are the following:

- $\omega_1 = \omega_2 = \omega_p$ pump frequency

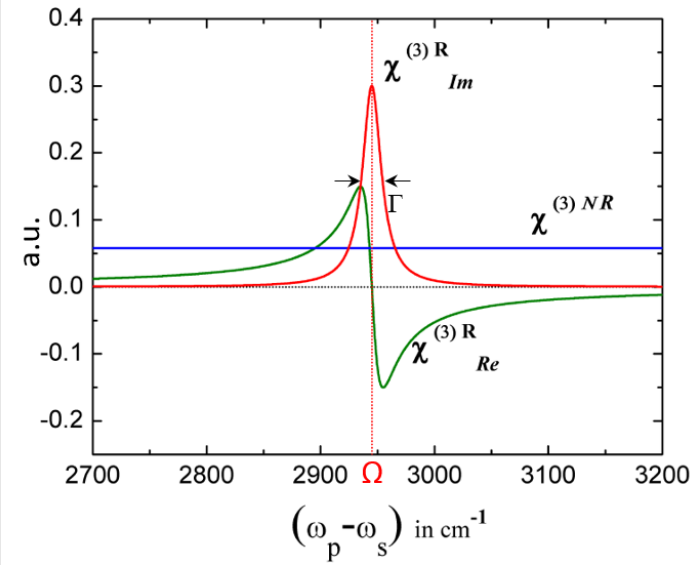

Figure 1.4: Example of plot of the resonant (real and imaginary) and non-resonant part of the third-order nonlinear susceptibility.

- $\omega_3 = \omega_4 = \omega_S$ Stokes frequency

It is fundamental to note that in this case the phase-matching condition $\Delta k = k_4 + k_2 - k_3 - k_1 = 0$ is always satisfied. We can than write the Eq. 1.84 for the Stokes beam and for the pump beam

$$\frac{dA_S}{dz} = -i\alpha_S \chi^{(3)} |A_p|^2 A_S \tag{1.89a}$$

$$\frac{dA_p}{dz} = -i\alpha_p \chi^{(3)} |A_S|^2 A_p \tag{1.89b}$$

In the hypothesis of no pump depletion ($A_p \cong const$), assuming an input Stokes beam such that $A_S(0) = A_{S0}$ and integrating Eq 1.89b we obtain

$$A_S(L) = A_{S0} \exp(-i\alpha_S \chi^{(3)} |A_p|^2 L). \tag{1.90}$$

In the small gain limit(which is satisfied in SRS with signal of 10^{-4} or less), we can expand Eq 1.90 and it becomes

$$A_S(L) \cong A_{S0} - i\alpha_S \chi^{(3)} |A_p|^2 A_{S0} L = A_{S0} + \Delta A_S \tag{1.91}$$

$$\text{with} \qquad \Delta A_S = -i\alpha_S \chi^{(3)} |A_p|^2 A_{S0} L \ll A_{S0} \tag{1.92}$$

that corresponds to an intensity of the Stokes beam on the detector of

$$I_S(L) \cong |A_S(L)|^2 = |A_{S0} + \Delta A_S|^2 \tag{1.93}$$

Remembering the rule

$$|a+b|^2 = |a|^2 + |b|^2 + 2\,\mathrm{Re}\{a^* b\} \tag{1.94}$$

with a and b complex numbers and with Eq 1.92, we obtain

$$\begin{aligned} I_S(L) = |A_{S0} + \Delta A_S|^2 = |A_{S0}|^2 + |\Delta A_S|^2 + 2\,\mathrm{Re}\{A_{S0}^* \Delta A_S\} \cong \\ \cong |A_{S0}|^2 + 2\,\mathrm{Re}\{A_{S0}^* \Delta A_S\} \end{aligned} \tag{1.95}$$

This configuration is known as **self-heterodyning** effect where the SRS signal is amplified by the Stokes field. Since $\Delta A_S = -i\alpha_S \chi^{(3)} |A_p|^2 A_{S0} L$ we can write

$$\begin{aligned} I_S = I_{S0} + 2\,\mathrm{Re}\{-i I_{S0} I_p L (\mathrm{Re}\{\chi_R^{(3)}\} + i\,\mathrm{Im}\{\chi_R^{(3)}\} + \chi_{NR}^{(3)})\} \\ \Longrightarrow I_S = I_{S0} + \alpha_S\,\mathrm{Im}\{\chi_R^{(3)}\} I_{S0} I_p L \end{aligned} \tag{1.96}$$

In practice what is measured is the **Stimulated Raman Gain (SRG)**

$$SRG = \frac{\Delta I_S}{I_{S0}} = \alpha_S\,\mathrm{Im}\{\chi_R^{(3)}\} I_p L \tag{1.97}$$

In the same way one can obtain

$$I_p = I_{p0} - \alpha_p\,\mathrm{Im}\{\chi_R^{(3)}\} I_{p0} I_S L \tag{1.98}$$

and measure the **Stimulated Raman Loss (SRL)**

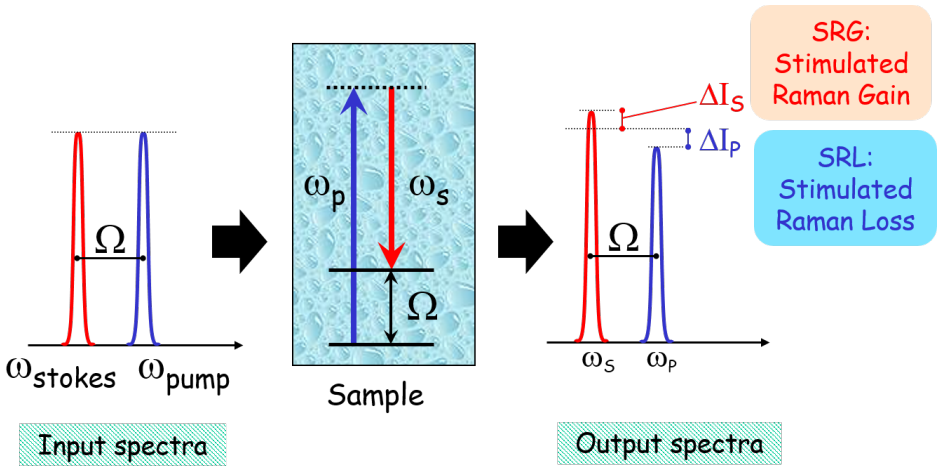

Figure 1.5: Stimulated Raman Gain(SRG) and Stimulated Raman Loss(SRL)

$$SRL = \frac{\Delta I_p}{I_{p0}} = -\alpha_p \,\mathrm{Im}\{\chi_R^{(3)}\} I_S L \tag{1.99}$$

The above calculations show us that the information we accede is the imaginary part of the resonant third-order non linear susceptibility. After some calculations, in this configuration the SNR (Rignal to Noise Ratio) may be written as[4]:

$$SNR_{SRS} \propto \frac{2\,\mathrm{Im}\{\chi_R^{(3)}\}] I_p I_S}{\alpha I_S + \sqrt{I_S}} \overset{\alpha=0}{\Rightarrow} 2\,\mathrm{Im}\{\chi_R^{(3)}\} I_p \sqrt{I_S} \tag{1.100}$$

where αI_S denotes the laser intensity noise of the Stokes beam, and $\sqrt{I_S}$ is the shot noise (i.e. the intrinsic statistical uncertainty of the measured light due to Poissonian distribution of photon counts within a certain time window) of the probe beam intensity. Owing to high-frequency demodulation detection(needed to remove the large linear background on which the signal lies), αI_S can be removed and it is possoble to reach the shot-noise limit. We can summarize the SRS advantages as follows:

- it is inherently phase-matched
- since it measures the imaginary part of $\chi^{(3)}$ it suppresses all the non-

resonant contributions(given by $\chi^{(3)}_{NR}$) which is real

- since $\chi^{(3)} \propto N$(number of molecules) the signal scales linearly with the number of oscillators in the focal volume, making it simpler to detect less abundant species

On the other hand, the major disadvantage is that the signal ΔI_S sits on a larger background which is generally noisy: sophisticated high-frequency demodulation techniques are needed.

1.4.2 Coherent Antistokes Raman scattering (CARS)

In CARS the vibrational coherence is created in the same way of SRS but it is read by a further interaction with the pump beam, generating a coherent radiation at the anti-Stokes frequency, $\omega_{aS} = \omega_p + \Omega$ as shown in Fig 1.6 The overall process can be seen like a split of two pump photons into two photons of higher and lower energy, with energy being conserved.

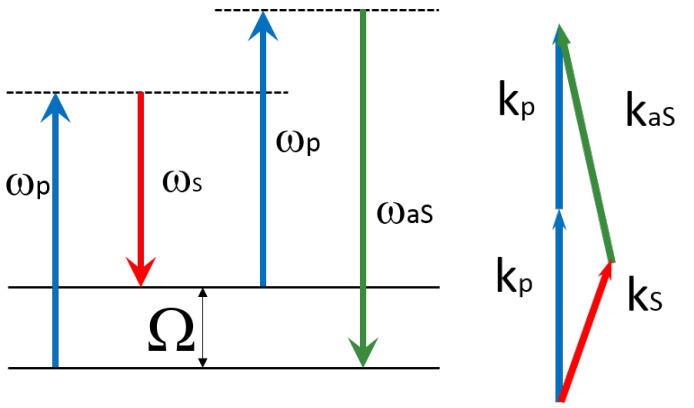

(a) Frequency diagram of CARS.

(b) Phase-matching condition for CARS.

Figure 1.6: The anti-Stokes radiation is blueshifted with respect to pump and Stokes frequencies.

For CARS the hypothesis are:

- $\omega_1 = \omega_3 = \omega_p$ pump frequency

- $\omega_2 = \omega_S$ Stokes frequency
- $\omega_4 = \omega_{aS} = 2\omega_p - \omega_S$ anti-Stokes frequency

We further assume that there is not large variation of pump and Stokes beam (i.e. $A_p \cong cost$ and $A_S \cong cost$). We obtain than from Eq. 1.84d the equation for the anti-Stokes field

$$\frac{dA_4}{dz} = -i\alpha_4\chi^{(3)}A_p^2A_S^*\exp[i\Delta kz] \tag{1.101}$$

which has the solution

$$A_{CARS}(L) = -i\alpha_{aS}\chi^{(3)}A_p^2A_S^*L\exp(i\Delta kL)\frac{\sin(\Delta kL/2)}{\Delta kL/2}. \tag{1.102}$$

We detect the intensity of the CARS signal that is

$$I_{CARS} = |A_{aS}|^2 = \alpha_{aS}^2|\chi^{(3)}|^2I_p^2I_SL^2\,\mathrm{sinc}^2(\Delta kL/2) \tag{1.103}$$

Now we make the assumption $\Delta kL \cong 0$, that is well satisfied in microscopy because of tight focusing. So $\mathrm{sinc}^2(\Delta kL/2) \approx 1$ and

$$I_{CARS} \propto |\chi^{(3)}|^2I_p^2I_SL^2 \tag{1.104}$$

Using again the rule Eq 1.94 we can write

$$I_{CARS} \propto |\chi^{(3)}|^2 = |\chi_R^{(3)}+\chi_{NR}^{(3)}|^2 = |\chi_R^{(3)}|^2+|\chi_{NR}^{(3)}|^2+2\chi_{NR}^{(3)}\,\mathrm{Re}\{\chi_R^{(3)}\} \tag{1.105}$$

We can estimate the CARS SNR in the scenario of dilute analytes [4] (i.e. $|\chi_R^{(3)}|^2 \ll |\chi_{NR}^{(3)}|^2$)

$$SNR_{CARS} \propto \frac{2\chi_{NR}^{(3)}\,\mathrm{Re}\{\chi_R^{(3)}\}I_p^2I_S}{\alpha|\chi_{NR}^{(3)}|^2I_p^2I_S+\chi_{NR}^{(3)}I_pI_S} \overset{\alpha=0}{\Rightarrow} 2\,\mathrm{Re}\{\chi_R^{(3)}\}I_p\sqrt{I_S} \tag{1.106}$$

where $\alpha|\chi_{NR}^{(3)}|^2I_p^2I_S$ denotes the low-frequency intensity noise carried by the

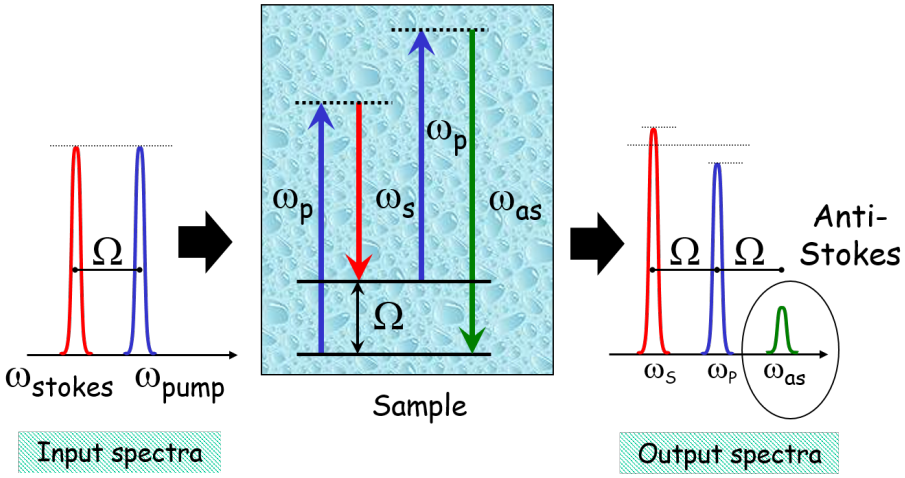

Figure 1.7: CARS process and generation of anti-Stokes frequency.

nonresonant background due to the $1/f$ noise of the excitation lasers, and $\chi^{(3)}_{NR} I_p I_S$ is the shot noise of the nonreosonant background. The shot-noise limit is reached only in the ideal situation in which α is vanishing. It is worth noting that $SNR_{CARS}|_{\alpha=0}$ is approximately equal to $SNR_{SRS}|_{\alpha=0}$ in the ideal situation in which laser intensity fluctuation can be eliminated completely and the shot noise is the only remaining noise source.

According to above formulas we can understand that CARS, with respect to SRS, is inherently free from linear background of Stokes beam because signal is isolated from the input fields, which are hence easy to filter out. On the other hand we also see that many problems are present:

- significant spectral-shape distortion due to the presence of frequency independent Non-Resonant Background(NRB) given by $\chi^{(3)}_{NR}$and the interference between resonant and non-resonant contributions(see Fig1.8) $(2\chi^{(3)}_{NR}\,\mathrm{Re}\{\chi^{(3)}_R\})$
- even in the absence of NRB, $I_{CARS} \propto N^2$ scales as the square of molecular concentration, making it difficult to detect less abundant molecules

The effect of NRB is the major limitation in CARS measurements and this

is the reason why many techniques of NRB suppression have been developed.

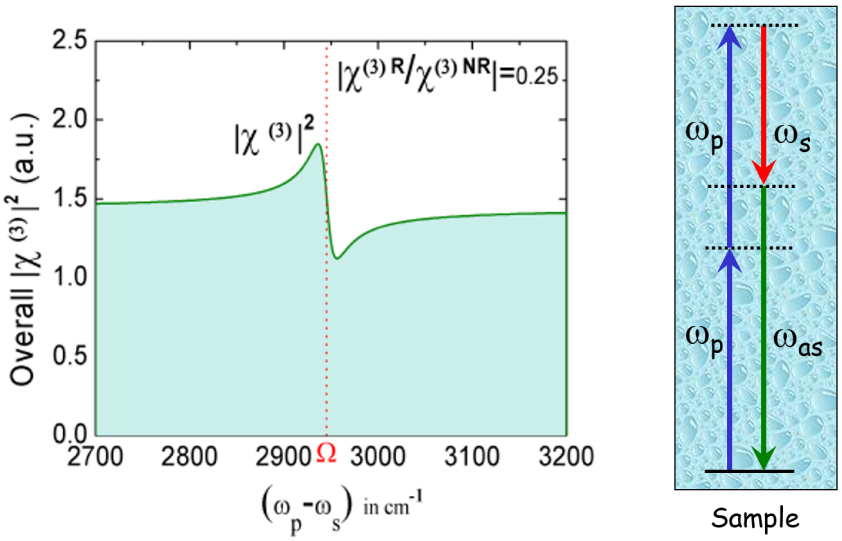

(a) Example of CARS signal where distorition provided by NRB is clearly visible.

(b) Example of four wave mixing process.

Figure 1.8: In figure (a) it is shown how a signal distorted by NRB looks. In (b) the energy diagram of one of the possible NRB makeups.

1.4.3 NRB suppression techniques

In this section we will briefly describe the most important Non-Resonant Background suppression techniques which are:

1. *Interferometric (or heterodyne-detected) CARS (iCARS)*
2. *Frequency-modulation CARS (FM-CARS)*
3. *Time-resolved CARS*
4. *Polarization CARS (P-CARS)*

Interferometric (or heterodyne-detected) CARS (iCARS)

In the iCARS approach[5] we mix a local oscillator (LO) at the anti-Stokes frequency with the CARS signal. The two fields must be phase-locked.

$$I_{TOT} = |E_{CARS} + E_{LO}\exp(i\Delta\phi)|^2 = |-i\beta(\chi_R^{(3)} + \chi_{NR}^{(3)}) + E_{LO}\exp(i\Delta\phi)|^2 \tag{1.107}$$

Developing the square and neglecting the CARS intensity with respect to that of LO we obtain

$$I_{TOT} = |E_{LO}|^2 - 2\beta E_{LO}(\mathrm{Re}\{\chi_R^{(3)}\} + \chi_{NR}^{(3)})\cos(\Delta\phi) - 2\beta E_{LO}(\mathrm{Im}\{\chi_R^{(3)}\}\sin(\Delta\phi) \tag{1.108}$$

An important consequence of Eq. 1.108 is that the real and the imaginary contributions to the signal now exhibit different dependencies on $\Delta\phi$. If we set $\Delta\phi = 90°(0°)$ we maximize the resonant imaginary part (real part) and the mixing term, containing the nonresonant response, vanishes. As only vibrationally resonant signals give rise to imaginary signal components, heterodyne probing of $\mathrm{Im}\{\chi_R^{(3)}\}$ allows background-free detection. In addition, the detected signal is linear in the concentration of vibrational modes, which allows for direct concentration measurements. Furthermore interferometric CARS enables linear amplification by increasing the amplitude of the local oscillator. The major issue with iCARS, as for FM-CARS, is the requirement of three different independently tunable phase-locked narrowband pulses (pump, Stokes, LO), making this technique very arduous to realize.

Frequency Modulation CARS (FM-CARS)

Let us consider an isolated resonance centered at a frequency Ω. Imagine now to probe this vibrational mode with a narrowband source; if the probing source is rapidly swapped between two frequency ω_S and $\omega_{S'}$ with a frequency difference $\delta = \omega_S - \omega_{S'}$, we have a frequency modulation that results in an amplitude modulation of the CARS signal[6] (Fig 1.9):

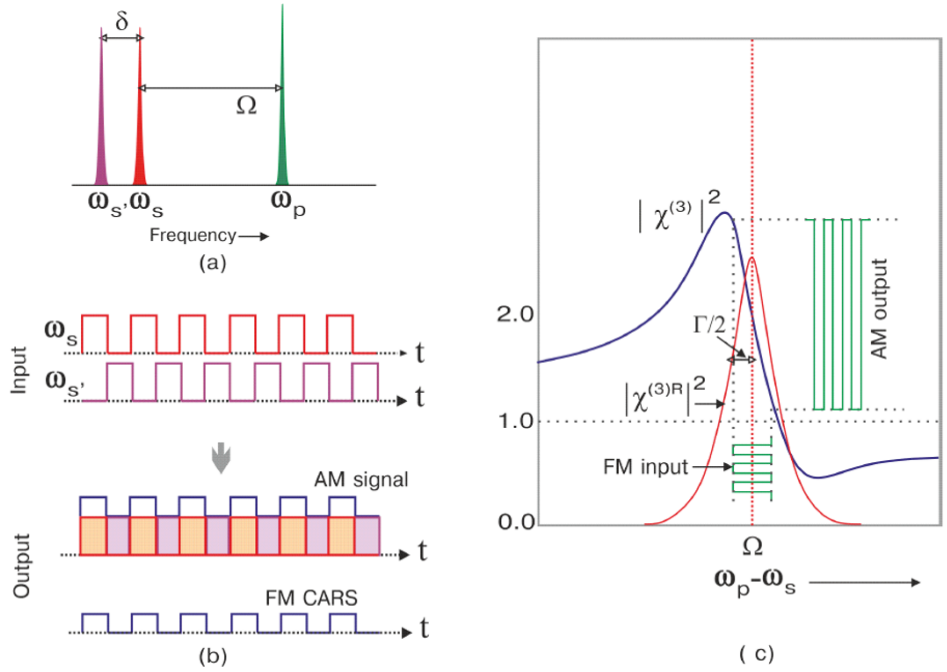

Figure 1.9: FM-CARS outline.

$$\Delta I(\delta) = I(\omega_S) - I(\omega_{S'}) \tag{1.109}$$

Since NRB is spectrally flat, this modulation allows to efficiently suppress it by subtracting the spectra recorded within and out of resonance through the use of a lock-in detection. FM CARS is most advantageous when the resonant signal is comparable with or smaller than the nonresonant background. This measurement requires three different independently tunable narrowband pulses (pump, Stokes 1, Stokes 2) and a very complicated detection system, making it very difficult to implement.

Time-Resolved CARS

The Time-resolved CARS[7] relies on the fact that Raman coherence, created by temporally-overlapped pump/Stokes pulse-pair and read out by a probe field (usually the pump again), has a dephasing time of the order of picosecond,

related to the spectral width of the corresponding Raman band while NRB exhibits instantaneous dephasing time(i.e., it is present only when the three fields are temporally overlapped).

It means that, if we delay the probe pulse with respect to pump and Stokes, the NRB disappears(Fig. 1.10). Again the requirements of three synchronized phase-locked laser colors brings back up to the drawbacks of iCARS and FM-CARS.

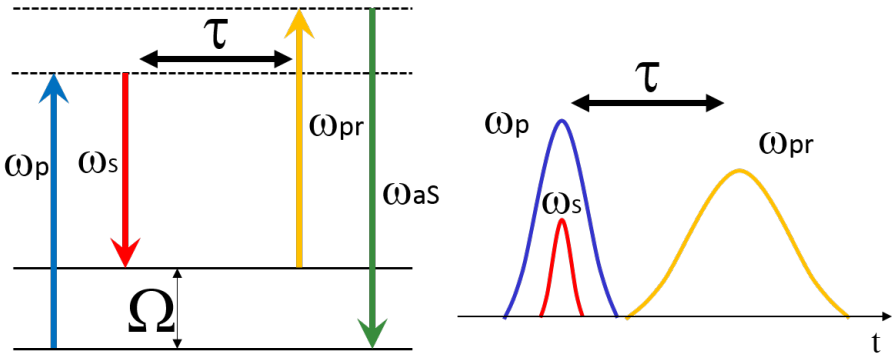

(a) Frequency scheme of TR-CARS. (b) Time scheme of TR-CARS

Figure 1.10: TR-CARS

Polarization-Sensitive CARS (P-CARS)

P-CARS[8] can provide high vibrational contrast by suppressing the non-resonant background through the polarization difference between resonant $P_R^{(3)}$ and nonresonant(electronic) $P_{NR}^{(3)}$ contribution to the signal. The theory of P-CARS takes into account the tensor nature of third-order nonlinear susceptibility and it can be found elsewhere[9](a hint of this $\chi^{(3)}$ behavior will be given in section 1.3.4). Here the aim is just to give an outline of the process. The polarization direction of the emitted CARS field is determined by the polarization of the incident pump and Stokes fields and the Raman

depolarization ratio ρ (i.e. the intensity ratio between the perpendicular component and the parallel component of the Raman scattered light) of the material. The depolarization ratio of the resonant signal ρ_R depends on the molecular vibrational mode and usually differs from the constant depolarization ratio of the isotropic non-resonant background ρ_{NR}. With linearly-polarized(but not collinear) pump and Stokes beams, a difference between ρ_R and ρ_{NR} leads to non-parallel, linearly-polarized resonant and non-resonant anti-Stokes fields. In polarization-sensitive CARS, a polarization analyzer in front of the detector blocks the non-resonant signal, whereas a portion of the differently polarized resonant signal leaks through the analyzer placed orthogonally with respect to the non-resonant signal. The detected resonant signal is optimized when the polarization difference between $P_R^{(3)}$ and $P_{NR}^{(3)}$ is maximized.

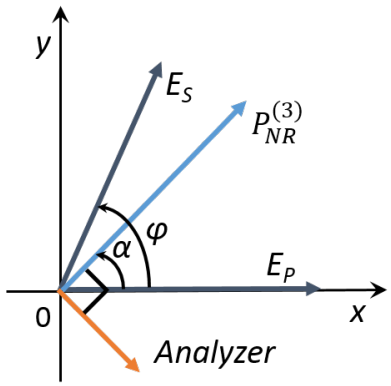

Figure 1.11: Possible configuration of P-CARS

In the configuration shown in Fig 1.11 the optimal angles for maximization of resonant signal are $\alpha = 45°$ and $\varphi = 71.6°$[8]. The major disadvantage of this approach is that it's possible to collect only the projection of resonant signal on the analyzer direction,which is usually very weak.

1.4.4 Raman-Induced Kerr Effect (RIKE)

RIKE[10] relies on the Raman-induced birefringence that occurs when the pump-Stokes frequency detuning is in resonance with a vibrational transition, leading to a polarization change of the Stokes (pump) field. Like for SRS, in RIKE, the generated emission is thus at the excitation frequencies. In SRS, this radiation is emitted parallel to the excitation field, and in RIKE, the emission is polarized perpendicular to the excitation fields. In this aspect, RIKE is similar to CARS, as the emitted radiation does not interfere with the excitation light, while in SRS interference of the new emission results in intensity gain or loss of the excitation fields.

As shown in section 1.2 the polarization of the sample can be written as a power series of the excitation fields. The general expression for the third order contribution at the frequency ω_4 is[10]

$$P^{(3)}(\omega_4) = \chi^{(3)}(\omega_4;\omega_1,\omega_2,\omega_3) \cdot E(\omega_1) \cdot E(\omega_2) \cdot E(\omega_3) \tag{1.110}$$

where as usual $\chi^{(3)}(\omega_4;\omega_1,\omega_2,\omega_3)$ is the the nonlinear optical susceptibility and $E(\omega_1)$,$E(\omega_2)$ and $E(\omega_3)$ are the electric fields of the excitation beams at frequency ω_1, ω_2 and ω_3. This nonlinear polarization further has to be treated as a tensor $\chi^{(3)}_{\alpha\beta\gamma\delta}$ in which α,β,γ and δ are the indexes of the polarization components of the electrical fields $E_\alpha(\omega_1)$,$E_\beta(\omega_2)$,$E_\gamma(\omega_3)$ and $E_\delta(\omega_4)$. Depending on the symmetry of the system, only certain combinations are allowed. Specifically, in isotropic samples $\chi^{(3)}_{1111}$, $\chi^{(3)}_{1122}$, $\chi^{(3)}_{1212}$ and $\chi^{(3)}_{1221}$ and their permutations are the only nonvanishing elements. In the original implantation of SRS, parallel and linearly polarized excitation fields are used and so features of $\chi^{(3)}_{1111}$ are measured[10](see Fig.1.12). It is straightforward to also measure features of $\chi^{(3)}_{1221}$ by using linearly polarized pump and Stokes beams with perpendicular polarization. Traditionally, two different beam geometries are used: one employs a linearly polarized Stokes beam at a 45° angle with respect to pump beam (known as linear RIKE), the other uses a circularly polarized Stokes beam (known as circular RIKE).The RIKE nonlinear polarization at the pump frequency is proportional to $\chi^{(3)}_{1122} + \chi^{(3)}_{1212}$

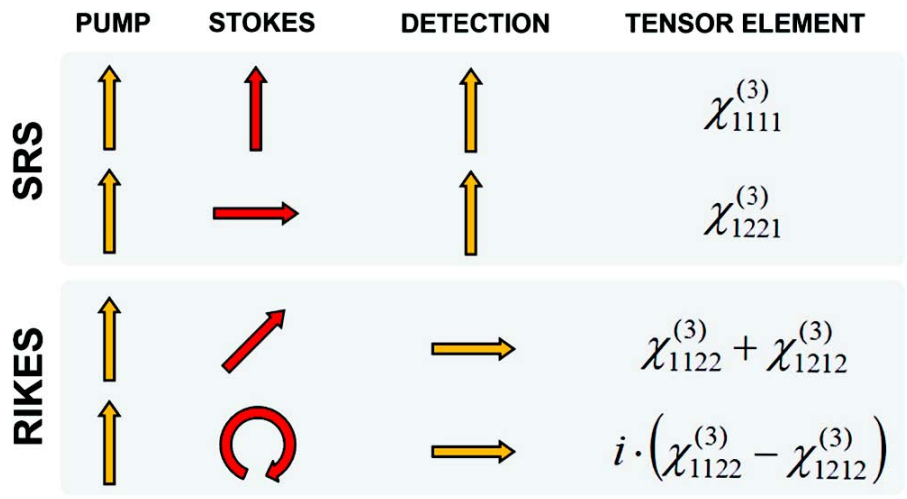

Figure 1.12: Polarization configurations for SRS and RIKE of the pump beam. The first two columns show the polarization of the excitation fields (pump and Stokes) and the third column the orientation of a polarizer in front of the detector, which is sensitive for the pump beam only. Configurations in which detection is along the polarization of the pump beam are referred to as SRS, and configurations in which detection is perpendicular to the polarization of the pump beam as RIKE. Due to the four nonvanishing elements of nonlinear polarization tensor only the four configurations shown here generate a signal. RIKE requires the Stokes beam to have polarizations along both polarization axes. The fourth column indicates the specific tensor elements that are probed.

for the linear RIKE and $i(\chi^{(3)}_{1122} - \chi^{(3)}_{1212})$ in case of the circularly RIKE, where i indicates that the polarization is phase-shifted by 90° with respect to the phase of the pump beam[10](see figure 1.12).

Thus, the combination of SRS and RIKE microscopy can probe the distribution of all important tensor elements of the nonlinear susceptibility in the sample.

1.5 Broadband CRS

With *Broadband* it is meant that the Stokes pulse is an ultrashort, hence ultrabroadband, femtosecond pulse whose bandwidth is about 100-200nm

(∼1000-2000cm^{-1}) or even more.

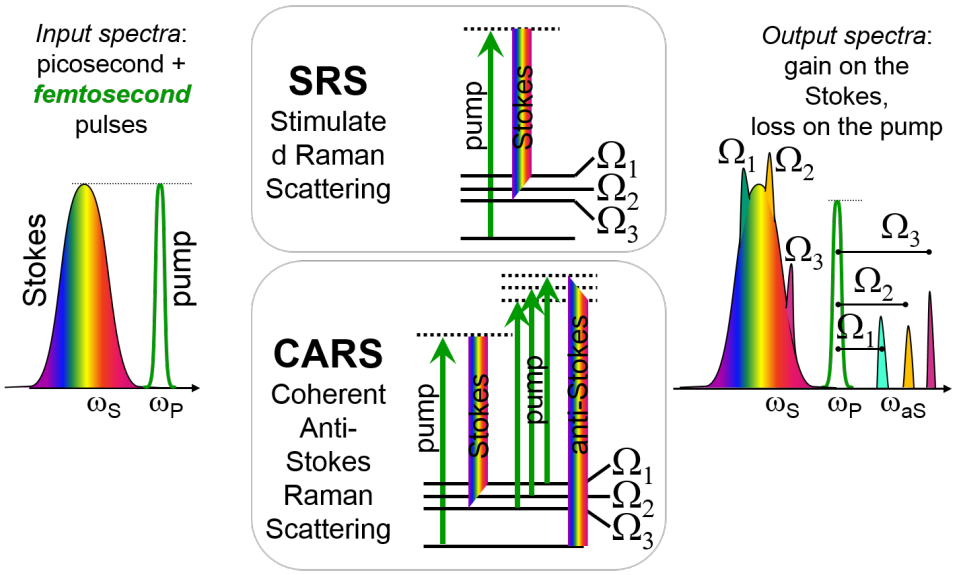

Figure 1.13: Boradband CRS processes.

As shown in Fig. 1.13 the principles is exactly the same of single-colour CRS, in fact in BSRS the vibrational frequencies will show up as peaks on top of the Stokes spectrum while in BCARS as peaks on the anti-Stokes background-free blue-shifted side. All the problems related to CARS and SRS discussed in the previous sections (such as NRB for CARS or linear-background subtraction with SRS) remains unaffected.

Of course the great advantages of such techniques is that within a single pulse there are all the pursued information about the investigated sample, but on the other hand the detection is much more difficult than the single color one. Indeed, with single colour experiments the a single photodiode can be used, whereas with broadband configuration a more sophisticated detectors are needed. For frequency domain detection dispersive detectors as spectrometer or monochromator are needed in order to disperse all the spectral component within the signal. For time domain detection single channel detectors can be used but before the signal must coupled into an interferometer in order to recover spectra after Fourier Transform of interferogram trace.

Chapter 2

Broadband CARS

In this chapter I will discuss Broadband CARS, starting from the laser system, until the different physical processes involved. Afterwards experimental data will be discussed.

2.1 Laser System

2.1.1 Erbium Fiber Laser and EDFA

Erbium Fiber Laser

A fiber laser is a laser in which the active gain medium is an optical fiber doped with rare-earth elements such as erbium, ytterbium, neodymium, dysprosium, praseodymium, and thulium.

Erbium (chemical symbol: Er) is widely used in the form of the trivalent ion Er^{3+} as the laser-active dopant of gain media based on various host materials, including both crystals and glasses. Erbium-doped glasses, mostly of silicate and phosphate types, are used both for bulk lasers and fiber lasers and amplifiers. The most common laser transition (also widely used in erbium-doped fiber amplifiers) is that from the $^4I_{13/2}$ manifold to the ground-state manifold $^4I_{15/2}$(Fig 2.1). Depending on the glass composition, the transition wavelength is usually between 1.53 and 1.6 μm. Because this is a quasi-three-level transition, erbium-doped laser and amplifiers require a

significant excitation density of the erbium ions, and erbium lasers typically exhibit a high lasing threshold.

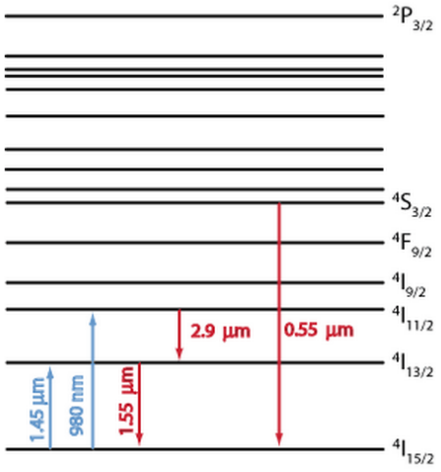

Figure 2.1: Energy level structure of the trivalent erbium ion, and some common optical transitions.

The most common pump scheme is based on the transition $^4I_{15/2} \rightarrow ^4I_{11/2}$ with a wavelength around 0.9–1 μm, although in-band pumping ($^4I_{15/2} \rightarrow ^4I_{13/2}$ e.g. at 1.45 μm) is also possible. A multi-phonon transition, which is relatively fast in silicate glasses (due to their high phonon energies), leads from $^4I_{11/2}$ to $^4I_{13/2}$. The upper-state lifetime of $^4I_{11/2}$ is of the order of 8–10 ms, whereas all higher-lying levels have lifetimes of at most a few microseconds due to fast multi-phonon decay.

EDFA

Erbium-doped fiber amplifiers are by far the most important fiber amplifiers in the context of long-range optical fiber communications; they can efficiently amplify light in the μm wavelength region, where telecom fibers have their minimal losses.

A typical setup of a simple erbium-doped fiber amplifier (EDFA) is shown in Fig. 2.2. Its core is the erbium-doped optical fiber, which is typically a single-mode fiber. In the shown case, the active fiber is "pumped" with light from two laser diodes (bidirectional pumping), although unidirectional pumping in the forward or backward direction (co-directional and counter-directional pumping) is also very common. The pump light, which most often has a wavelength around 980 nm and sometimes around 1450 nm, excites the erbium ions into the $^4I_{13/2}$ state (in the case of 980-nm pumping via $^4I_{11/2}$), from where they can amplify light in the 1.5-μm wavelength region

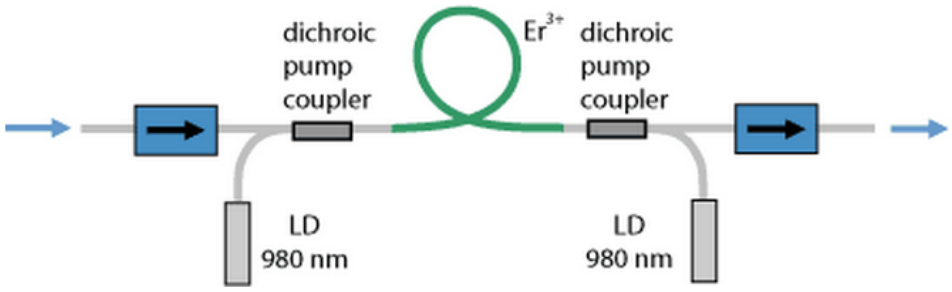

Figure 2.2: Schematic setup of a simple erbium-doped fiber amplifier. Two laser diodes (LDs) provide the pump power for the erbium-doped fiber. The pump light is injected via dichroic fiber couplers. Pig-tailed optical isolators reduce the sensitivity of the device to back-reflections.

via stimulated emission back to the ground-state manifold $^4I_{15/2}$(Fig. 2.1).

The setup shown also contains two "pig-tailed" (fiber-coupled) optical isolators. The isolator at the input prevents light originating from amplified spontaneous emission from disturbing any previous stages, whereas that at the output suppresses lasing (or possibly even destruction) if output light is reflected back to the amplifier. Without isolators, fiber amplifiers can be sensitive to back-reflections.

2.1.2 Toptica Source

The principal source we used to perform CRS is a 40-MHz mode-locked Erbium-doped fiber oscillator with two amplified branches (Toptica, Femto-Promodel), both delivering nearly ≈70 fs long pulses at 1550 nm and 350 mW average power. As the two branches share the same seed source, they are synchronized with attosecond precision[11].

In one branch, to generate the pump pulses, the fundamental output of the amplifier is focused in a periodically poled lithium niobate (PPLN) crystal for second-harmonic generation. A crystal length of 10 mm is used to generate flattop pulses of 0.6 nm bandwidth, 3 ps duration, 200 fs rise time, close to the Transform-limit condition. The bandwidth corresponds to 10 wavenumbers, which matches the typical linewidths of vibrational bands in

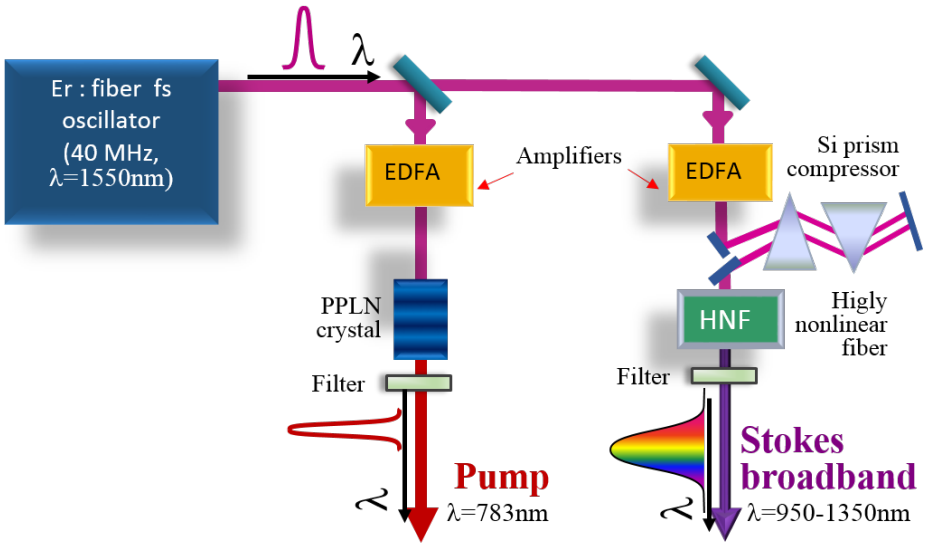

Figure 2.3: Layout of Toptica laser source.

the condensed phase, and allows us to obtain high-resolution spectra. Average powers of 50 mW are obtained at 783nm(λ_p).

In the other branch the fundamental input at 1550 nm is coupled with an higly non linear fiber and is split into two components[12] . The dispersive wave shifts toward the visible, and the solitonic wave (which is filtered out for our purposes) tunes toward longer wavelengths. Adjustment of the input chirp of the driving pulses by translating one prism in the Si compressor allows us to set the center wavelength of the two components. The bandwidth of the dispersive wave amounts to 350 nm properly centered at 1120 nm(λ_S). Whit this configuration we are able to achieve a coverage of Raman shifts from 0 (this is true only in the condition of Trasform-limited Stokes pulse, otherwise a if the pulse is chirped this is the 0 wavenumber are no longer accessible) to $\sim$3100 cm^{-1}. The average power amounts to 13 mW. The full scheme is shown in Fig. 2.3.

2.2 Broadband CARS setup and processes

2.2.1 Set-up

Two synchronized and spatially overlapped pulses, exiting from the system described before (broadband Stokes with ≈20fs duration and narrow-band pump with ≈2ps duration) are focused onto the sample. The spatial and temporal superpositions are provided using a Dichroic Beam Splitter(DBS) and a delay line lying on the Stokes beam path, respectively(Fig. 2.4).

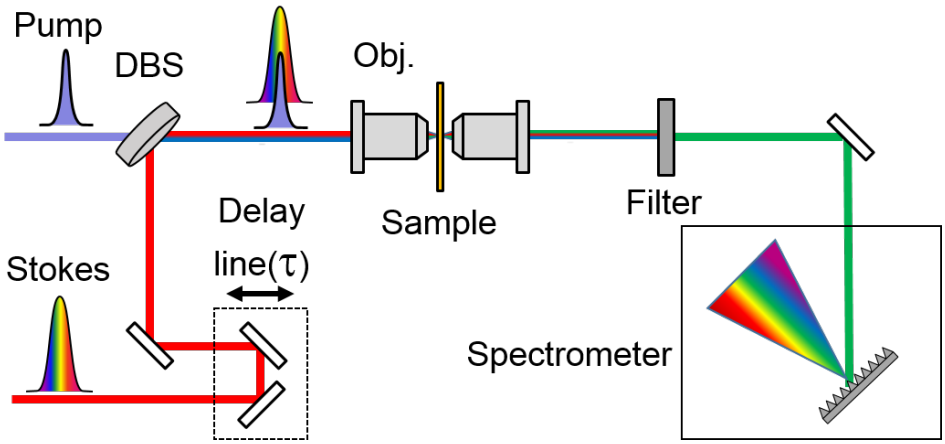

Figure 2.4: CARS set-up. DBS dichroich beam splitter, Obj. objectives

After the interaction with the sample, within the beam are present three contributions: the remaining pump and Stokes and the CARS signal. For this reason, and knowing that CARS signal is blue-shifted with respect to the excitation light, a short-wave-pass filter is placed after the sample. In this way, only the light at anti-Stokes frequency is transmitted and it can be detected with a spectrometer, as shown in Fig 2.4.

2.2.2 Two-color and Three-color CARS

The developed system uses two different excitation methods[1], two-color(2C) and three-color(3C) CARS[1]. These mechanisms operate simultaneously as they are simply different permutations of the same two pulses, but their

effect differ significantly.

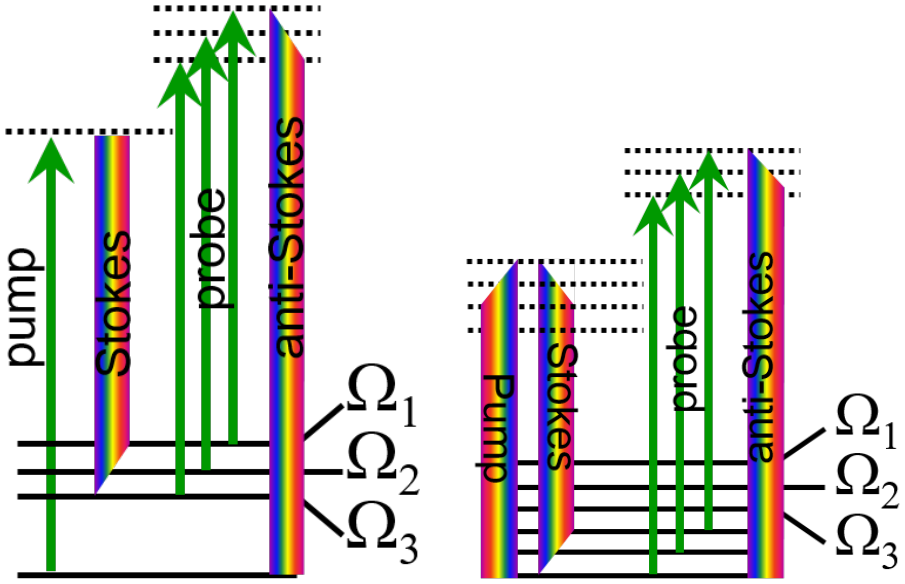

(a) Two-colour(2C) CARS. (b) Three-colour(3C) CARS.

Figure 2.5: Broadband CARS excitation mechanisms.

To illustrate this, we begin with an expression for the frequency-domain CARS signal intensity, $I_{CARS}(\omega)$[1]:

$$I_{CARS}(\omega) \propto |\{\chi^{(3)}(\omega)[E_S(\omega) \star E_p(\omega)] * E_{pr}(\omega)\}|^2 \tag{2.1}$$

where ω is the frequency, $\chi^{(3)}$ is the third-order nonlinear susceptibility, $E_S(\omega)$, $E_p(\omega)$,$E_{pr}(\omega)$ are the pump, Stokes and probe fields, respectively, and $\star$ and $*$ are the cross-correlation and convolution operators. The term in square brackets is the frequency-domain coherence generation profile, which will maximize at the frequency difference between the peaks of the pump and Stokes fields.

Assuming real, Gaussian fields, the integrated spectral intensity over all frequencies is given as[1]:

$$\langle I_{CARS} \rangle \propto P_p P_S P_{pr} \frac{\sigma_p \sigma_S \sigma_{pr}}{\sqrt{\sigma_p^2 + \sigma_S^2 + \sigma_{pr}^2}} \tag{2.2}$$

where P_p, P_p, P_{pr} are respectively the pump, Stokes and probe spectrally integrated modulus-squared field (proportional to the average power), such that $P = \langle |E|^2 \rangle = |E_0^2| \sqrt{\pi}\sigma$ where E_0 is th field envelope amplitude with $1/e$ half-width σ.

Under two-colour (2C) excitation (Fig. 2.5(a)), with degenerate pump and probe sources ($P_{p,pr} \equiv P_p = P_{pr}$;$\sigma_{p,pr} \equiv \sigma_p = \sigma_{pr}$) the BCARS signal resolution is provided by the narrowband pump–probe source, and the spectral breadth is provided by the Stokes source. Thus, from Eq2.2[1],

$$\langle I_{2C} \rangle \propto P_{p,pr}^2 P_S \frac{\sigma_{p,pr}^2 \sigma_S}{\sqrt{2\sigma_{p,pr}^2 + \sigma_S^2}} \approx P_{p,pr}^2 P_S \sigma_{p,pr}^2 \tag{2.3}$$

For intrapulse three-color (3C) excitation (Fig. 2.5(b)) in which the probe is independent and the SC provides the pump and Stokes photons($P_{p,S} \equiv P_p = P_S$;$\sigma_{p,S} \equiv \sigma_p = \sigma_S$)[1]:

$$\langle I_{3C} \rangle \propto P_{p,S}^2 P_{pr} \frac{\sigma_{p,S}^2 \sigma_{pr}}{\sqrt{2\sigma_{p,S}^2 + \sigma_{pr}^2}} \approx P_{p,S}^2 P_{pr} \sigma_{p,S} \sigma_{pr} \tag{2.4}$$

We note two important differences between these coherence generation mechanisms. One is that the two-colour mechanism has a peak excitation profile at the difference frequency between the narrowband and SC pulses (near 2,800cm^{-1} for our system), whereas the intrapulse three-colour mechanism has a peak excitation frequency at 0cm^{-1}, because the pump and Stokes fields are degenerate. Thus, the former excites the CH/OH stretch region, which typically presents an intrinsically stronger response, whereas the latter excites the fingerprint region, with the weaker intrinsic response.

The other important difference between these mechanisms is their efficiency over a broad bandwidth. With two-colour excitation, as described in Eq. 2.3, the total CARS signal is independent of the Stokes source bandwidth σ_S.Thus, with increasing σ_S, the total integrated CARS signal remains con-

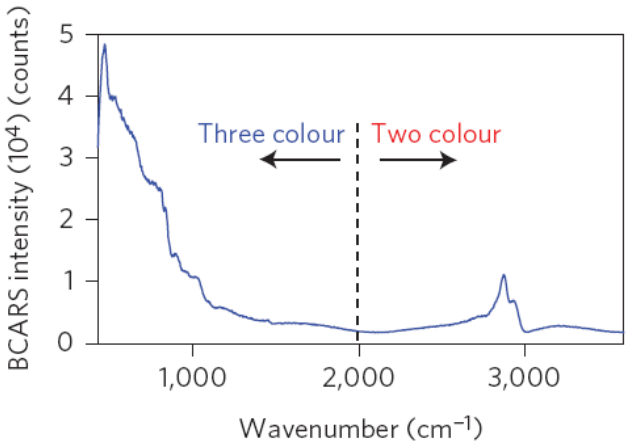

Figure 2.6: Example of Broadband CARS spectrum where are depicted the two-colour and three-colour CARS regions[1].

stant, but the signal at each spectral increment will decrease. In contrast, as described in Eq. 2.4, the total three-colour CARS signal rises with increasing bandwidth $\sigma_{p,S}$. Importantly, the signal at each spectral increment also increases with increasing $\sigma_{p,S}$. From this comparison, one can appreciate that the three-color mechanism is much more efficient than the two-color mechanism for this kind of system.

We can quantify the relative efficiency as

$$\langle I_{3C} \rangle / \langle I_{2C} \rangle \propto \sigma_S / \sigma_{pr} \approx 100 \tag{2.5}$$

So this system provides strong and efficient excitation within the fingerprint region.

2.3 Experimental results

The spectrum used to perform Broadband CARS measurement and the time-resolved excitation scheme are shown in Fig. 2.7.

The spectra that will be shown were collected with an HR2000 OCEAN OPTICS Spectrometer with 10ms integration time and with 20x objectives(excitation NA=0.65, collection NA=0.4). These spectra are from 1mm

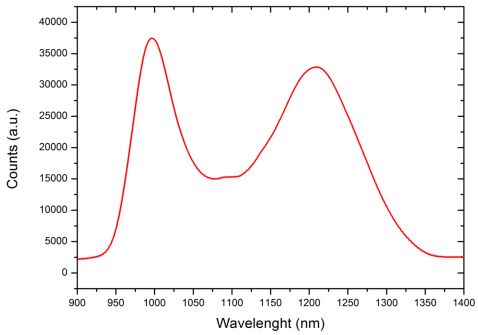

(a) Stokes spectrum.

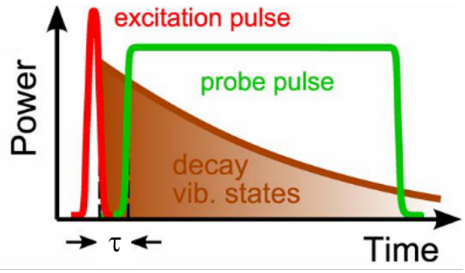

(b) Time-resolved excitation scheme[11].

Figure 2.7: Stokes spectrum.

thick plate of PMMA (Poly-methyl methacrylate) and they will be classified with respect to delay between the two excitation pulses. The one labeled as *Zero delay* were collected in condition of complete superposition between the Stokes and pump pulses. In contrast, the one labeled as *Big delay* were acquired in condition of partial temporal superposition Fig. 2.7(b). This has been done to evidence the role of Non-resonant background.

Indeed, as shown in Fig2.8 the spectral collected with *zero delay*, are completely overwhelmed by NRB making impossible to recognize the typical Raman peaks belonging to PMMA. On the contrary in the *big delay*, Fig2.9 spectrum is possible to recognize some peaks, in particular in the fingerprint(three-colour CARS), but not in the CH-stretching region(two-colour CARS).

In the *zero delay* spectrum the main contribution is given by the instantaneous four-wave mixing which is the source of NRB. It is clear that when the delay between pulses increases, the Raman features of specimen start to come out from the NRB, also thanks to the heterodyne amplification provided by the NRB.

These spectra shown here are preliminary data and the development of such set-up in ongoing. Of course to retrieve complete and clean imaginary part of the non-linear susceptibility from a BCARS spectrum the so called time-domain Kramers–Kronig transform (TDKK)[1][13] should be performed

in order to extract only the resonant signal.

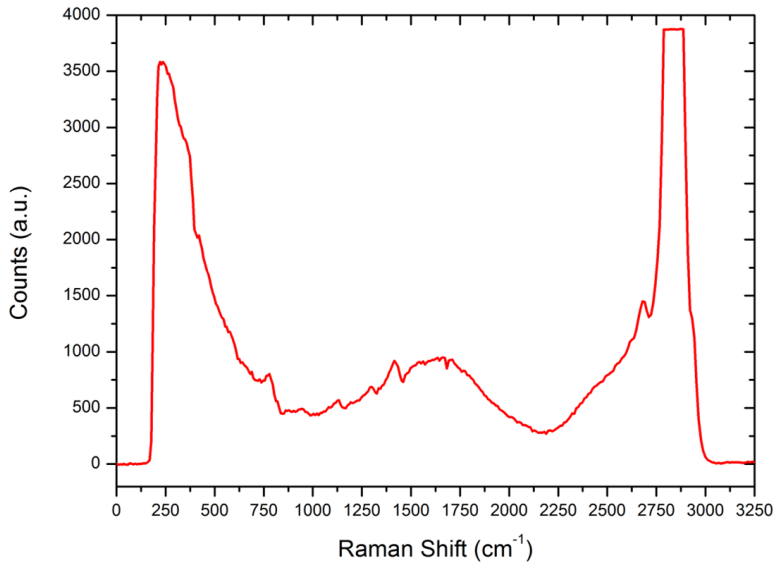

Figure 2.8: *Zero delay* spectrum.

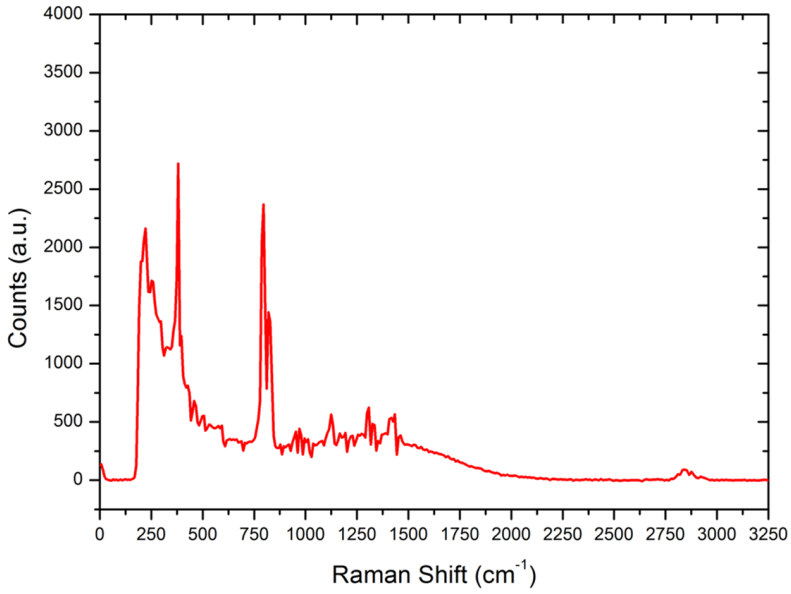

Figure 2.9: Big delay spectrum.

Chapter 3

Broadband SRS

In this chapter, a new kind of approach for Broadband (or multi-color) SRS will be shown, in particular a *time domain* (or *Fourier Transform*) implementation through the use of a special kind of interferometer. This has been done with a novel optical configuration called **TWINS** (Translating-Wedge-Based Identical Pulses eNcoding System) which solves in a simple, compact and cost-effective way the problem of building a collinear delay line with interferometric stability. Afterwards the experimental data will be analyzed and discussed.

3.1 Introduction

Stimulated Raman Scattering is a third-order technique, as already explained in Chapter 1, involving a pump and a Stokes beam overlap in time and space at the sample. For particular energy differences between pump and Stokes frequencies, the SRS process creates a gain on the Stokes and anti-Stokes sides, which reflect the spectra of the sample under investigation. On the anti-Stokes side is the CARS signal, which is a homodyne signal, with the advantage of being background free but with also the consequence of having a quadratic dependence with the signal strength. On the Stokes side is the SRS signal, which is self-heterodyne by the Stokes beam, and thus has linear dependence with the signal size, but it is a small signal lying on top

of a strong Stokes beam, which requires highly sensitive detection. At the frequency of the pump, there is a Raman loss process.

Only a few experimental demonstrations of broadband SRS spectroscopy and microscopy have been presented so far. They can be grouped into two main categories. The first employs narrowband pump and Stokes pulses at the frequencies ω_p and ω_S respectively, resonant with a single vibrational frequency $\Omega = \omega_p - \omega_S$. Subsequently, tuning the spectrum of one of the two beams allows one to access other vibrational frequencies; stacking the data, one can thus reconstruct an entire multispectral image. This scheme has been demonstrated both tuning the spectrum line by line[14] and frame by frame (using two synchronized laser sources and a wavelength scanner in a 4-f scheme[15]). The tuning range was however intrinsically narrow ($\approx$300cm^{-1}) due to the limited achievable tuning range of the laser.

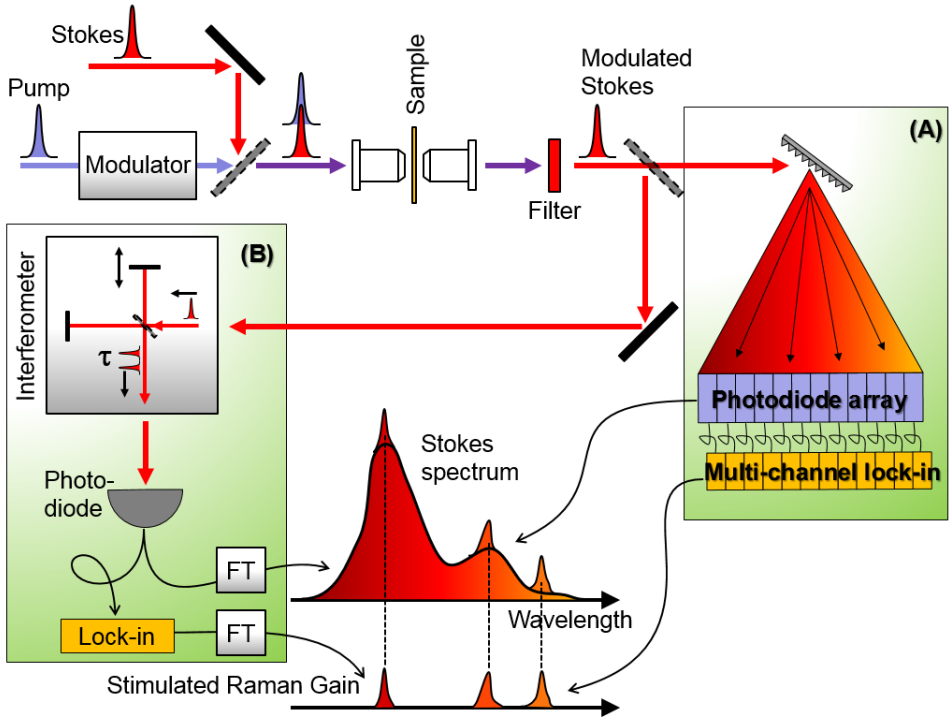

Figure 3.1: Conceptual scheme for broadband SRS in the standard (A) and FT (B) implementations.

The second approach to multiplex SRS employs a broadband Stokes pulse to collect the SRS signal at the same time from all the vibrational frequencies(see Fig. 3.1(A)) The intensity of the pump beam is modulated at high speed (ideally at a frequency equal to half the repetition rate of the laser to take advantage of the lower 1/f noise) using either an acousto-optical modulator or an electro-optical modulator. The two beams are collinearly overlapped using a dichroic beam splitter and focused on the sample through the same objective. Temporal overlap of the two pulses on the sample is controlled by an optical delay line on one of the two arms. Modulation transfer occurs on the broadband Stokes at those wavelengths corresponding to stimulated Raman gain with respect to the wavelength of the pump in the presence of a specific molecular vibration. After the sample (in the case of a measurement in transmission) a filter rejects the pump photons and the Stokes spectrum detected. In the usual case, the pump photons are at higher energies with respect to the Stokes ones, so that one measures the SRG on the Stokes spectrum as in Fig. 3.1. In the opposite case, one measures SRL on the Stokes in a process also known as Inverse Raman scattering[16]. On the one hand this method is more powerful with respect to the one based on narrowband pulses because it does not require to tune the laser, which is always limited in both speed and spectral coverage, but on the other the multi-color detection is often challenging.

There are several proposed experimental schemes using the approach based on a broadband Stokes pulse. They employ a multi-channel photodiode array, where each channel is physically connected to a sub-unit of a multi-channel lock-in amplifier[17]. This solution is very powerful, but it is complex from the electronics point of view and its implementation generally extremely expensive, making it difficult to be applied for mainstream biological applications. Another earlier implementation used a spectrometer equipped with a CCD/CMOS/NMOS linear image sensor[18]. This solution is mainly limited by the full-well capacity of the pixels, of the order of 10^6 electrons, which reduces the achievable signal-to-noise ratio to $\Delta\tilde{I}_S/\tilde{I}_S = 10^{-3}$ or less for a single spectrum (depending on the number of photons illuminating each pixel)). As the read-out speed typically cannot exceed a few kilohertz, it

would require several seconds or even minutes to achieve a sensitivity down to $\Delta\tilde{I}_S/\tilde{I}_S = 10^{-5}$ needed for most applications.

3.2 Principle of measurement

Here it is proposed a radically different approach (see Fig. 3.1(B)) which requires a single photodiode and a usual single-channel lock-in amplifier. It makes use of the time-domain measurement of spectra enabled by Fourier-Transform spectroscopy, in analogy with the FTIR[19] technique used in the mid-infrared region, where dispersive elements and multi-channel detectors are not readily available.

The Stokes beam after the sample with (complex) electric field $E_S(t) = A_S(t)e^{i\omega_0 t}$ is sent to a linear interferometer, (such as a Michelson) that creates two collinear equal replicas of the pulse to be characterized $E_S(t)$ and $E_S(t-\tau) = A_S(t-\tau)e^{i\omega_0(t-\tau)}$, where τ is the relative temporal delay between them. The beam is sent to a single-channel slow photodetector, which measures the time-integrated energy $U(\tau)$ of the two pulses for any given delay τ:

$$\begin{aligned} U(\tau) = \int_{-\infty}^{+\infty} |E_S(t) + E_S(t-\tau)|^2 \, dt = \int_{-\infty}^{+\infty} |A_S(t)|^2 \, dt + \\ \int_{-\infty}^{+\infty} |A_S(t-\tau)|^2 \, dt + 2e^{i\omega_0 t} \int_{-\infty}^{+\infty} A_S(t) A_S^*(t-\tau) \, dt + c.c. \end{aligned} \tag{3.1}$$

The first two terms are constant and equal to the total energy of the pulses. The third depends on the delay τ, and it can be written as $2|C_A(\tau)| \cos[\omega_0\tau + \Phi(\tau)]$, where:

$$C_A(\tau) = \int_{-\infty}^{+\infty} A_S(t) A_S^*(t-\tau) \, dt = |C_A(\tau)| e^{i\Phi(\tau)} \tag{3.2}$$

is the linear (field) autocorrelation of the Stokes pulse. Following the Wiener-Khinchin theorem $\tilde{C}_A(\omega) = |\tilde{A}_S|^2$: the Fourier transform $\tilde{C}_A(\omega)$ with respect to τ of the field autocorrelation $C_A(\tau)$ is equal to $|\tilde{A}_S|^2$ which is the

spectrum of $E_S(t)$.

This is illustrated in Fig. 3.1(B) , where the Stokes spectrum is retrieved by scanning the delay τ and by numerically compute the Fourier transform of the signal collected by the photodiode. With respect to this well-known procedure, at the basis of FTIR spectrometers[19], we add high-speed lock-in detection before the Fourier transformation to directly retrieve the pump-induced spectral changes of the Stokes spectrum. If we now consider the variation induced by the pump on the Stokes field we have $E_S(t) = E_{S0}(t) + \Delta E_S(t)$ and consequently:

$$A_S(t) = A_{S0}(t) + \Delta A_S(t) \quad \text{with} \Delta A_S \ll A_{S0}$$
$$|A_S(t)|^2 = |A_S(t)|^2 + |\Delta A_S(t)|^2 + 2Re\{A_S(t)\Delta A_S^*(t)\}$$

Neglecting the dependence on the square variation of the form $|\Delta A_S(t)|^2$ and calculating again the integral (3.1) we obtain:

$$\begin{aligned}
U'(\tau) &= \int_{-\infty}^{+\infty} |A_{S0}(t)|^2\, dt + \int_{-\infty}^{+\infty} |A_{S0}(t-\tau)|^2\, dt + \\
&+ \int_{-\infty}^{+\infty} 2Re\{A_{S0}(t)\Delta A_S^*(t)\}\, dt + \int_{-\infty}^{+\infty} 2Re\{A_{S0}(t-\tau)\Delta A_S^*(t-\tau)\}\, dt + \\
&+ 2e^{i\omega_0 t} \int_{-\infty}^{+\infty} [(A_{S0}(t) + \Delta A_S)(A_{S0}^*(t-\tau) + \Delta A_{S0}^*(t-\tau))]\, dt + c.c. = \\
&= \int_{-\infty}^{+\infty} |A_{S0}(t)|^2\, dt + \int_{-\infty}^{+\infty} |A_{S0}(t-\tau)|^2\, dt + \\
&+ \int_{-\infty}^{+\infty} 2Re\{A_{S0}(t)\Delta A_S^*(t)\}\, dt + \int_{-\infty}^{+\infty} 2Re\{A_{S0}(t-\tau)\Delta A_S^*(t-\tau)\}\, dt + \\
&+ 2e^{i\omega_0 t} \int_{-\infty}^{+\infty} [A_{S0}(t)A_{S0}^*(t-\tau) + A_{S0}^*(t)\Delta A_S(t-\tau) + \Delta A_S(t)A_{S0}^*(t-\tau)] + c.c.
\end{aligned}$$

To retrieve completely only the signals relative to Raman vibrations we use a high speed lock-in detection, that makes the difference between the two signals $U(\tau)$ and $U'(\tau)$ through the use of an acousto-optic modulator, placed along the pump beam path.

$$\Delta U(\tau) = U(\tau) - U'(\tau) = \int_{-\infty}^{+\infty} 2Re\{A_{S0}(t-\tau)\Delta A_S^*(t-\tau)\} + \\ + 2e^{i\omega_0 t}\int_{-\infty}^{+\infty}[A_{S0}^*(t)\Delta A_S(t-\tau) + \Delta A_S(t)A_{S0}^*(t-\tau)]$$

The cross-correlation between two functions is defined as

$$C_C(t) = \int_{-\infty}^{+\infty} A(t)B^*(t-\tau)\,dt = (f \star g)(\tau)$$

If we perform now the Fourier Transform with respect toτ of $\Delta U(\tau)$ we finally get (the FT of cross-correlation is $\mathcal{F}[(f \star g)(\tau)] = \tilde{A}(\omega)\tilde{B^*}(\omega)$:

$$\Delta\tilde{U}(\omega) = 2[\tilde{A_S}(\omega-\omega_0)\Delta\tilde{A_S^*}(\omega-\omega_0) + \Delta\tilde{A_S}(\omega-\omega_0)\tilde{A_S^*}(\omega-\omega_0)] = \\ = 2Re\{\tilde{A_S}(\omega-\omega_0)\Delta\tilde{A_S^*}(\omega-\omega_0)\}$$

From theory[9] is known that we can express ΔA_S as a function of the material lenght L

$$\Delta A_S(L) = -i\chi^{(3)}\alpha_S A_{S0}|A_P|^2 L$$

$$\Delta U = 2Re\{A_{S0}\Delta A_S^*\} = 2Re\{i\chi^{(3)}\alpha_S|A_{S0}|^2|A_P|^2 L\}$$

Knowing that we can express $\chi^{(3)} = \chi_R^{(3)Re} + i\chi_R^{(3)Im} + \chi_N^{(3)}R$ the information we accede is the imaginary part of the Resonant third-order nonlinear susceptibility.

3.3 Broadband SRS Setup

First of all it is worth noting the high flexibility of our set-up. All the excitation scheme is almost identical to the one used for the Broadband CARS measurement. The differences are only in the modulation of the pump and after the interaction of the pulses with the samples, i.e. in detection scheme, with the so called TWINS interferometer, which i am going to discuss

in next section. Being the detection scheme the only difference between the SRS and CARS setup it was possible to choose the desired detection by only flipping one mirror.

3.3.1 TWINS interferometer

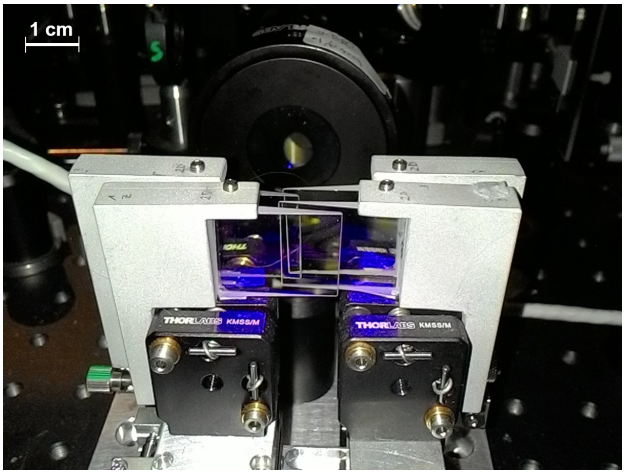

Figure 3.2: Picture of TWINS interferometer

TWINS principle

Now I introduce the the Translating-Wedge- Based Identical Pulses eNcoding System (TWINS)[20] as a simple and compact optical device generating two delayed, phase-locked collinear replicas of an input pulse. With the proper choice of materials, TWINS can be implemented in a broad range of wavelengths, from the ultraviolet to the mid-IR, and can work with sub-10 fs pulses. The interferometer is based on *Birefringence* whose discussion is remanded to Appendix A. This kind of interferometer is classified as a *common path interferometer*(i.e. the two replica of the pulse travel along the same path). Examples of these interferometers are the Sagnac interferometer and Fresnel's Biprism. TWINS has been widely used in particular in 2D spectroscopy[21, 22], where the constraint of phase-locked pulses and high interferometric stability is very rigid. If a pulse enters a birefringent plate

with polarization at 45° with respect to the ordinary and extraordinary axes, it splits into two perpendicularly polarized pulses of the same intensity, propagating with different group velocities. If the thickness of the birefringent plate is varied, which can be achieved by replacing the plate with a pair of wedges, then the delay between these two pulses will also be varied. Since the two pulse replicas follow the same optical path, they are phase-locked with very high stability and their delay can be controlled, with extreme precision and reproducibility, by changing the insertion of the birefringent wedges[20].

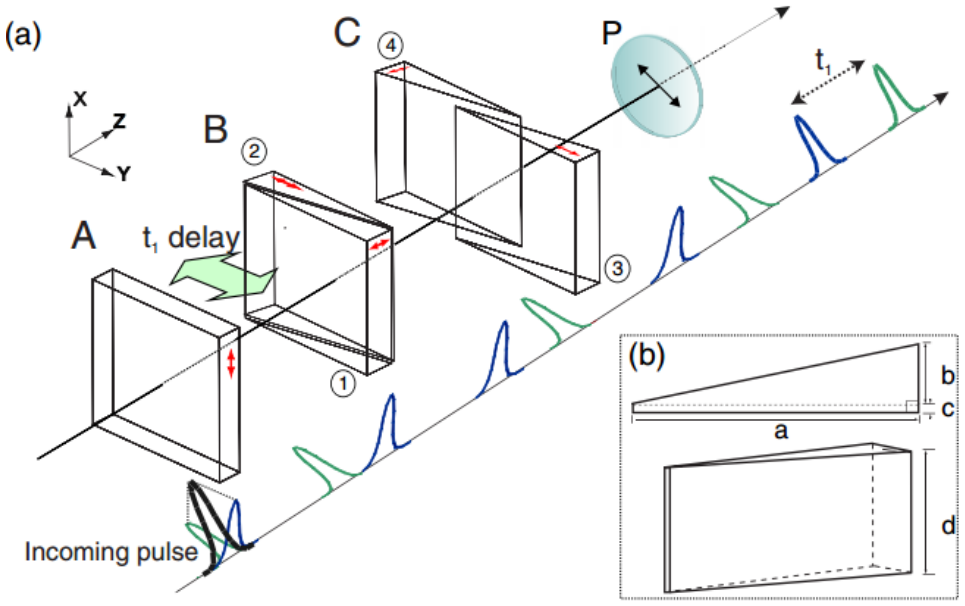

Figure 3.3: (a) Scheme of the TWINS setup. Block A creates a constant "negative" delay t1 between two orthogonally polarized pulses. Block B scans the delay $t_1$between the pump pulses towards positive time. Block C corrects angular dispersion and front tilt. Polarizer P projects the two pump pulses to a common polarization direction. Small arrows indicate the direction of the optical axis of the birefringent plates. The big arrow indicates the movement direction of block B.(b) wedge design, a = 25 mm, b = 3.1 mm, c = 0.5 mm, and d = 20 mm

Block A (Fig. 3.3)with its constant thickness compensate the overall

minimum delay introduced by blocks B and C. It introduces a constant delay for the Y-polarized pulse relative to the X-polarized one (see Fig3.3 for a definition X,Y,Z orientations) Due to the different orientations of the optical axes in the two wedges, the X-polarized pulse sees a constant optical path even when this block is moved into the beam, as the two wedges are geometrically identical. The Y-polarized pulse experiences a change in optical thickness, while block B is moved into the beam as depicted by the green arrow in Fig. 3.3. When using a negative birefringence material ($n_e < n_o$), increasing thickness of the birefringent wedge (wedge 2) decreases the optical path for the Y-polarized pulse, and this pulse arrives earlier than the X-polarized one. After exiting block B, the pulses are slightly non-collinear and front-tilted, because they experience different refractions at each interface, and because the phase front experiences different thickness of birefringent material. This is corrected by the static block C, consisting of two wedges identical to those in block B.

For our purpose , we can neglect the influence of the lateral displacement Δr (Fig 3.4) of the Y polarization relative to the X polarization, as the beam size (almost 1 cm) is significantly bigger than the maximal displacement ($\approx 200\mu$m)[21].

A polarizer placed at the end of the wedge sequence projects, if so required by the experimental configuration, the two pulses to a common polarization direction and can be removed if two orthogonally polarized pump pulses are required.

TWINS design, mounting and alignment procedure

For our purpose We used α-BaB_2O_4 (α-BBO) as a negative uniaxial birefringent material for the wedges. We distinguish Y-cut, Xcut, and Z-cut wedges by the orientation of their optical axis with respect to the coordinate system displayed in Fig. 3.3; one pair is Z-cut and the other is Y-cut. The sizes depend on the maximum delay one wants to achieve, the important parameter being the length of the b side(Fig. 3.3). The proper alignment of the TWINS device is a prerequisite to perform Broadband SRS.

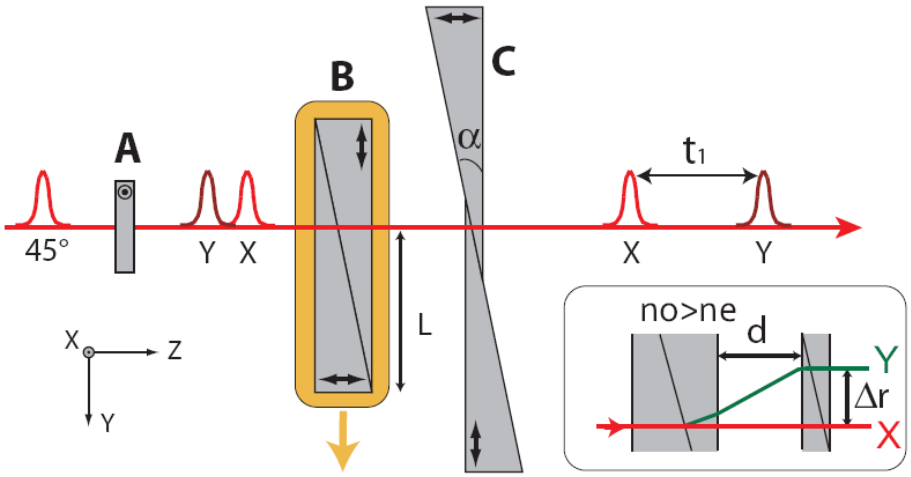

Figure 3.4: TWINS scheme seen from upside. In the inset is shown the path for X and Y-polarized beams inside the TWINS. Angles are exaggerated for clarity

The alignment and contrast optimization of the wedges is performed by using a large collimated He-Ne laser beam. First, we place block B into the beam. This way, the two orthogonally polarized components exit with different angles and are spatially separated after a few centimetres. We then set the input polarization to 45° by balancing the intensity of the two components. We insert the wedges of block C into the beam (with the translation stages, they can be easily inserted or removed).

TWINS advantages and characteristics

The main advantage of TWINS is its capability to generate a pair of phase-locked collinear Stokes pulses with delay which can be controlled to extreme precision even with standard motorized translation stages and without any feedback loop for active position control. One can calculate a gear ratio which corresponds to the ratio between the translation required to introduce a certain delay with the TWINS and the translation required with a standard interferometer in free space with a retroreflector. This gear ratio for α-BBO at 1000 nm and wedges with an apex angle of 7° is ≈ 60[20]. In fact, a motor

Table 3.1: α-BBO refractive indices $n_o$and n_e, birefringence Δn, Group velocity mismatch (GVM), and group velocity dispersion for ordinary and extraordinary axis (GVDo and GVDe).

λ nm	n_o	n_e	Δn	GVM (fs/mm)	GVDo (fs^2/mm)	GVDe (fs^2/mm)
1100	1.6573	1.5374	0.1199	402.5	37.8	16.6
900	1.6623	1.5410	0.1203	411.0	60.9	37.2
700	1.6674	1.5460	0.1215	427.1	91.3	61.0
500	1.6807	1.5557	0.1250	468.2	149.1	102
300	1.7342	1.5928	0.1414	672.6	391.5	260.7

resolution of 0.1 μm translates into a precision in delay of ≈50 attoseconds between the pulses. This extreme precision in delay control, combined with the phase-locking property of the pair of pulses exiting the TWINS setup (since both pulse replicas follow the same optical path, they are phase-locked with very high stability and reproducibility), open the way to fast scanning without the use of any tracking schemes, as would be required in other setups using conventional interferometers. The Sellmeier equations[23] allow us to calculate the maximum group delays achievable for a given thickness of the wedges, which are summarized in Tab3.1 for α-BBO at different wavelengths from near-IR to UV.

This delay is given by $\Delta t_{max} = \text{GVM}d$, where GVM is the group velocity mismatch between between ordinary v_{go} and extraordinary v_{go} polarizations

$$\text{GVM} = \frac{1}{v_{go}} - \frac{1}{v_{ge}} \tag{3.3}$$

and d is the thickness of birefringent material. With our wedge designs we can achieve group delay of ≈1.5 ps in the near-IR.

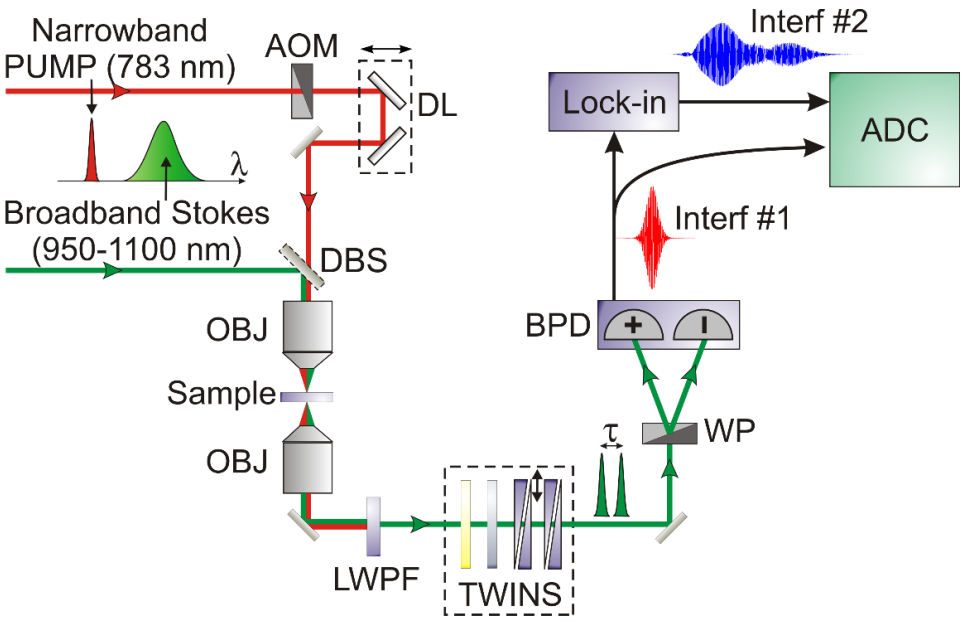

Figure 3.5: Set-up principle. AOM : Acousto-Optic Modulator. DL : Delay Line. OBJ: objectives. DBS : Dichroic beam splitter. LWPF: long wave èass filter. WP: Wollaston prism.

3.3.2 Set-up components

The Broadband SRS experiment was performed in the CH-stretching region and for our purpose, through the use of a slit present inside the arm of the laser, we cut the spectrum of the Broadband pulse in the longer wavelength part in order to have the maximum intensity in the CH-stretching spectral range that is, with a pump pulse at 783nm, around 1050nm(or $\sim$3000cm^{-1}). So our spectral coverage in this case was from 950nm to 1150nm($\approx$1800cm^{-1}).

As already shown in CARS measurement the spatial and temporal superposition of the beams is achieved through a delay line on the Stokes beam and a Dichroich Beam Splitter. The pump beam is acousto-optic modulated at 3 MHz. Afterwards the filtered Stokes from the sample is coupled into the TWINS interferometer. The input beam energy is equally distributed into two perpendicularly polarized components propagating on the two optical axes of birefringent wedges. The wedges' insertion into the beam permits to

apply an arbitrary delay between these two contributions, which are finally combined with a polarizer at the output. For our purpose we implemented:

Wollaston Polarizer and Balanced Detection As already mentioned a polarizer to make the two orthogonally polarized beams interfere is needed. A Wollaston prism, rotated by 45° with respect to the TWINS frame of reference, projects the two replicas onto two spatially separated beams with perpendicular polarizations. The two beams are sent to the photodiodes of a balanced detector in order to record two out-of-phase interferograms. This is done to cancel out the DC intensity and correlated noise of stokes beam and to double up the AC part(that is the interferogram).

MHz modulation and Lock-in detection With an acousto-optics modulator, we were able to modulate nearly 90% of the pump signal at 3 MHz of the SRS apparatus. During a wedge scan, we sent the balanced photodiode output to the fast lock-in, which contains only the signal of interest. Care has to be taken to sample the time-domain signals significantly slower than the modulated signals. We took care of demodulating the signal at a rate that permits to get sufficient sampling points of the time domain interferograms(≈100 points per fringes).

3.4 Experimental Results

3.4.1 Solvents

Here results obtained with various solvents will be shown. Fig. 3.6 reports experimental results performed on isopropanol solvent in a 1-mm cuvette. The interferogram directly measured by the photodiode is displayed in panel (a) as a function of the delay imposed by the TWINS between the two Stokes replicas. In the following, we will call it "Stokes interferogram" and we will denote it $I_S(t)$. The measurement is performed translating the two wedges of TWINS interferometer at constant speed without any feedback control on the position of the motor during the movement, as we verified that no

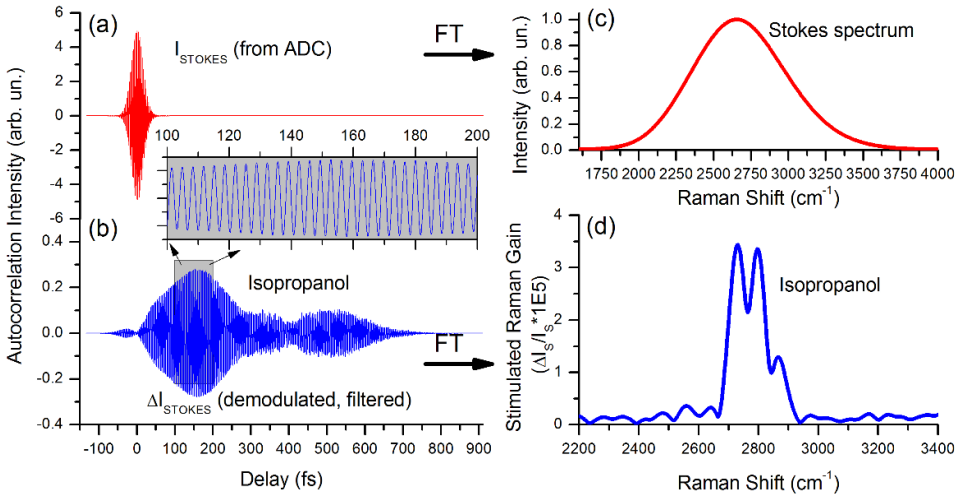

Figure 3.6: (a) interferogram of the Stokes pulse measured by scanning TWINS; (b) interferogram of the pump-induced Stokes intensity variation in isopropanol, demodulated by the lock-in amplifier; inset: zoom of the interferogram in the 100-200 fs region. (c) FT of (a), yielding the spectrum of the Stokes pulse; (d) SRG spectrum of methanol, obtained by normalizing the FT of (b) by the FT of (a).

significant deviation from linearity is present in the data. In this way the data collection can be set at constant sampling rate with no delay imposed by any feedback loop. The temporal position of the center of the interferogram varies around zero delay from scan to scan because the start event of data acquisition is not hardware triggered but only software triggered by the start event of the motor movement. For this reason, an automatic software routine centers the interferogram around time zero, taking advantage of its intrinsically symmetric profile. The same temporal shift is then imposed to the second interferogram simultaneously collected at the output of the lock-in, to guarantee its correct phasing (see Fig. 3.6(b)). In the following, we will call this the "SRS interferogram" and denote it $\Delta I_S(t)$. We apply a numerical bandpass filter centered at the carrier frequency of the Stokes pulse to both interferograms to remove excess noise. In the inset of Fig. 3(b) (gray area) we plot a lookup of the SRS interferogram, to demonstrate that we carefully sampled its oscillatory pattern well above the Nyquist limit. Note that, while

the Stokes interferogram has a vanishing oscillatory pattern at delays longer than ∼80 fs, the SRS interferogram displays strong signal for hundreds of femtoseconds. This can be explained either in the spectral domain or in the temporal domain: the broad and smooth Stokes spectrum, having a short temporal profile, after interaction with the pump-excited sample will display SRG in the form of narrowband Raman peaks (as discussed in Fig. 3.1), whose FT persists longer in time, for the well-known time-frequency reciprocity. It is also worth noting that all this data are available simultaneously.

The SRS interferogram is also symmetric around time zero; we only measure a single-sided SRS interferogram because the wedges have limited size and it is better to measure once up to longer delays rather than twice up to shorter delays. This also has the benefit of reducing the total measurement time. The use of balanced detection guarantees an excellent noise reduction only when the light on two photodiodes has equal intensity. For this reason, we reject the SRS interferogram around time zero, i.e. during the Stokes interferogram (in the ±80 fs interval). This is achieved multiplying the SRS trace by a Gaussian window function, with smooth transition from zero to one around time zero and viceversa from one to zero around 800 fs; this will guarantee a smooth FT, with reduced pedestals.

The Stokes spectrum $\tilde{I}_S$ is calculated by FT of the Stokes interferogram and is plotted in Fig. 3.6(c) as a function of its Raman shift with respect to the pump pulse (at 783 nm) in order to highlight the Raman spectral coverage of our setup, covering a vibrational spectrum as large as with approximately 1800cm^{-1} . In Fig. 3.6(d) we report the SRS spectrum of isopropanol $\Delta\tilde{I}_S(\omega)/\tilde{I}_S(\omega)$ calculated by normalizing the FT of the SRS interferogram, corresponding to $\Delta\tilde{I}_S(\omega)$ to the Stokes spectrum and taking into account a conversion factor equal to the employed input/output lock-in sensitivity. We note the presence of three clearly distinguished peaks at the vibrational frequencies 2870, 2930 and 3000 cm^{-1}, corresponding to the CH_3 symmetric stretch (at 2870cm^{-1}), the CH stretch (at 2930cm^{-1}) and the degeracy-lifted CH_3 asymmetric stretches (2990cm^{-1}) of isopropanol ($(CH_3)_2CHOH$)[24]. The integration time of the lock-in was set to 10ms, which limits the maximum translation speed of the wedges to 0.6mm/s to guarantee

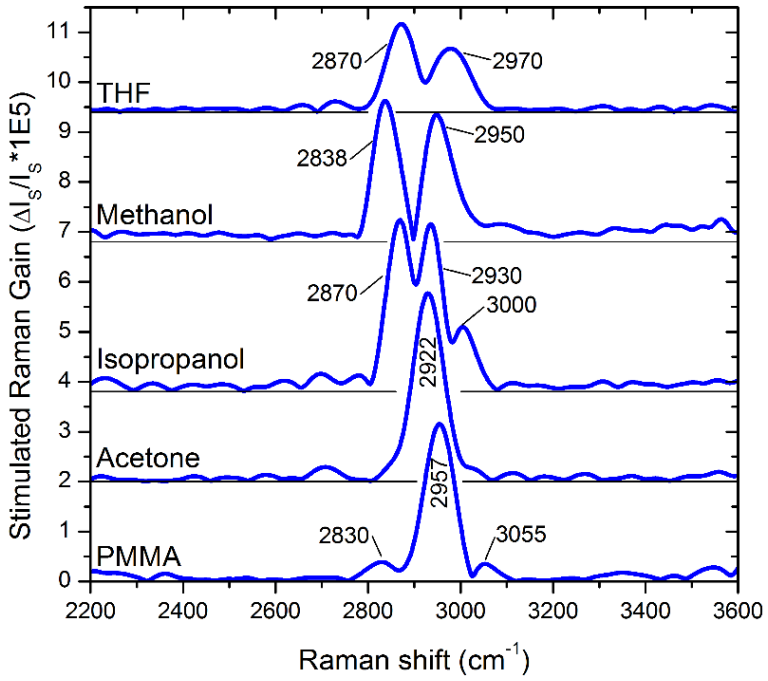

Figure 3.7: Broadband SRS spectra of different solvents and a PMMA film measured with FT technique.

sufficient sampling of the oscillation pattern at the Nyquist frequency thus resulting in a ≈37 seconds total measurement time[1]. The pump power was ∼7mW. The Stokes power was ∼5mW. The resulting maximum SRG signal is of the order of $\Delta\tilde{I}_S/\tilde{I}_S \sim 3 \cdot 10^{-5}$ and it sits on a $\sim 2 \cdot 10^{-6}$ noise floor. Similar results on other solvents (THF, methanol, acetone) and on a PMMA (polymethyl methacrylate) film are reported in Fig. 3.7.

[1]We work at 1μm wavelenght, which translates in the same value, multiplied for the wedge gear ratio (≈60⇒ 1μm·60=60μm)of motor movement to have an interference fringe. We acquire 10 points for every time constant of the lock-in so the movement of the wedges for every single collected point of interferogram is 6μm. So we can express the speed of the motor as $v_{wedges} = 6\mu\text{m}/T_{lock-in}$, where $T_{lock-in}$ is the time constant of the lock-in. This means that for 10ms of integration on the lock-in the speed is 0.6mm/s. So to cover all the excursion of the motor(22.5mm) the time taken is almost 37s.

3.4.2 Inorganic beads

We coupled our FT-SRS detection system to a home-made microscopic system to perform broadband coherent Raman imaging. We measured a mixture of PMMA and polystyrene (PS) spherical beads with 6μm and 3μm diameter, respectively, dispersed on a glass substrate. The sample is mounted on an X-Y-Z piezo stage (model number PI P-517.3CL) with sub-nanometer positioning precision. In this case we used an air-corrected 100x objective for focusing (model number, NA=0.75) and collection. The results are reported in Fig. 3.8. The imaged area has 21x21μm^2 size and was sampled using 140x140 pixels (thus resulting in a 150-nm pixel size). In this case the integration time per point was set at 1 s, resulting in a $\sim$1 second total measurement time per pixel. The measured three-dimensional dataset as a function of sample position and Raman shift can be decomposed in a series of images at various fixed vibrational frequency.

Fig. 3.8(a-c) reports three of them at 2910, 2956 and 3066cm^{-1} Raman shifts. In the image collected at 2956 cm^{-1} Raman shift (Fig. 3.8(b)) one can clearly see two intense circular areas with $\sim$6μm diameter, which correspond to two PMMA beads. Fig3.8(d) reports as a black solid line the entire Raman spectrum in the 2700-3200 cm^{-1} vibrational window measured in the center of one of these two spheres. It presents three clear Raman lines, as highlighted with small stars in Fig3.8(d), corresponding to the well-known signatures of PMMA. Five smaller disks with 3 µm diameter are visible in the image collected at 3066cm^{-1} Raman shift (Fig3.8(c)), which correspond to five PS beads. The corresponding Raman spectrum in the 2700-3200cm^{-1} vibrational window, as measured in the center of one of these five spheres, is reported in Fig. 3.8(d) reports as a red solid line. It presents three clear Raman lines, as highlighted with small stars, corresponding to the well-known signatures of PS in this wavenumber region. As an example, Fig3.8(a) reports the image collected at 2910 cm^{-1} Raman shift, where both materials display a weak Raman response so that it is possible to see their relative position. Note that single-color SRS, if tuned to this Raman line, would allow to detect both PMMA and PS beads but it does not suffice to distinguish them in general

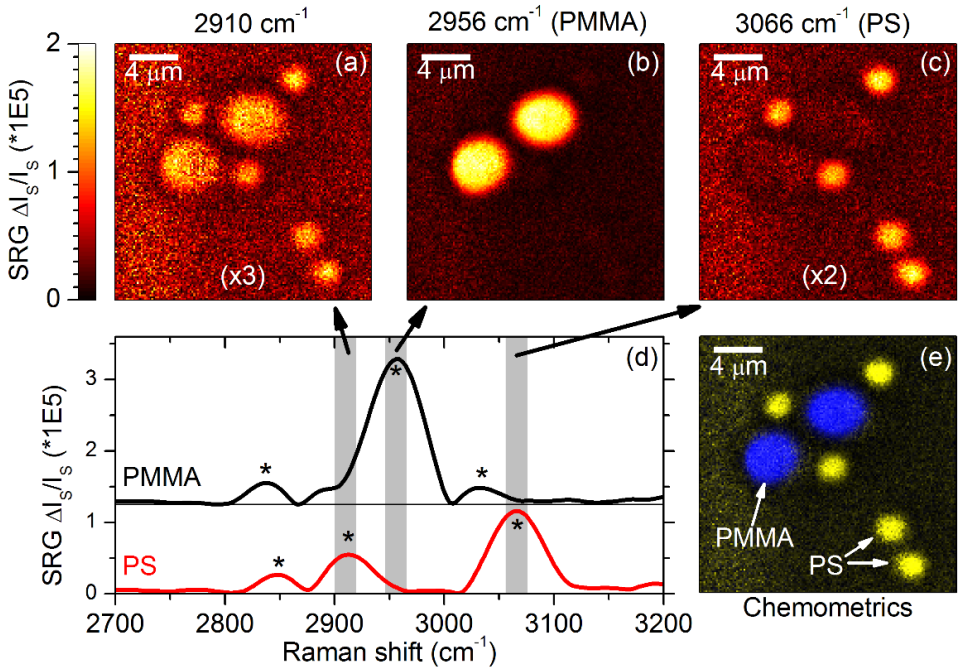

Figure 3.8: (a)-(c) Microscopic images of a mixture of 6-µm PMMA beads and 3μm m PS beads collected at different Raman frequencies: 2910 cm^{-1} (a) in partial resonance with both materials, 2956 cm^{-1} (b) in resonance with the PMMA beads, and 3066 cm^{-1}(c) in resonance with the PS beads. (d) Broadband SRG spectra collected in the center of a PMMA bead (upper black curve) and of a PS bead (lower red curve). Six stars indicate the proper identification of the three characteristic Raman peaks of both PMMA and of PS present in this high-frequency CH stretching region. Gray areas indicate the three spectral regions selected to plot the three images in panels (a)-(c). (e) Overlay image obtained using MCR-ALS algorithm.

(unless making use of their different size in this particular case).

We also analyzed our three-dimensional dataset using Multivariate Curve Resolution-Alternating Least Square (MCR-ALS) algorithm. MCR-ALS is a robust mathematical procedure to extract accurately the different species from a set of spectral data[25]. It can for example track the time evolution of transient species[26] and in the case of imaging, it can extract the position and concentration of species(Fig. 3.8(e)). It is based on SVD and Principal

Component Analysis (PCA), but has the additional flexibility that constraints can be used on the resulting spectra (like non-negativity of concentration and spectra). The dataset is decomposed in a set of spectra and concentration vectors, which product fits best the data matrix, excluding noise. MCR-ALS has a user-friendly Matlab interface that makes it attractive also to non-specialist[25].

3.5 Fourier Transform advantages and disadvantages

FT spectroscopy has been very popular in the infrared mainly because of the so-called multiplex advantages (Felgett's advantage)[27] which states that when the noise is dominated by the detector (which is the case with HgCdT detectors used in the IR), there is an advantage of using a multiplex detection with a single detector. This criterion is not valid in the visible or near IR, where the noise is dominated by the source (or shot noise), which is one of the reason why FT spectroscopy is not developed in the visible range. Worse, multiplexing becomes a disadvantage because noise from all the frequencies of the Stokes contributes together, even where there is no signal. In this regard, it would be better to measure the spectrum with a scanning spectrometer (grating + slits) with a single detector than doing the FT the way we do.

There are still some advantages of using FT, as the fact that the spectral resolution which can be tuned easily by changing the scan range without reducing the amount of light drastically like it is the case in a spectrometer with grating and slit. Another benefit of FT over dispersive spectrometer is throughput, as more light enters a FT spectrometer with respect to a scanning spectrometer(e.g. monochromator) because there is no slit. This is also true with our interferometer, but has to be moderated because we use of a pinhole at the entrance of the TWINS that permits to get better fringe contrast. In fact, in the TWINS, the two perpendicularly polarized beam do not exit exactly collinear, there is a small shift induced by the TWINS that

cannot be compensated in the present configuration[21]. The wedge size can limit the scan length of the time domain, and care has to be taken to scan delays long enough to reach the maximum resolution limit imposed by the pump bandwidth.

Undersampling

Another great advantage of Fourier Transform is the so called *Undersampling*. To *undersample* means to sample a signal at a sample rate below its Nyquist frequency (that is less than two time-points per period). If fewer data points

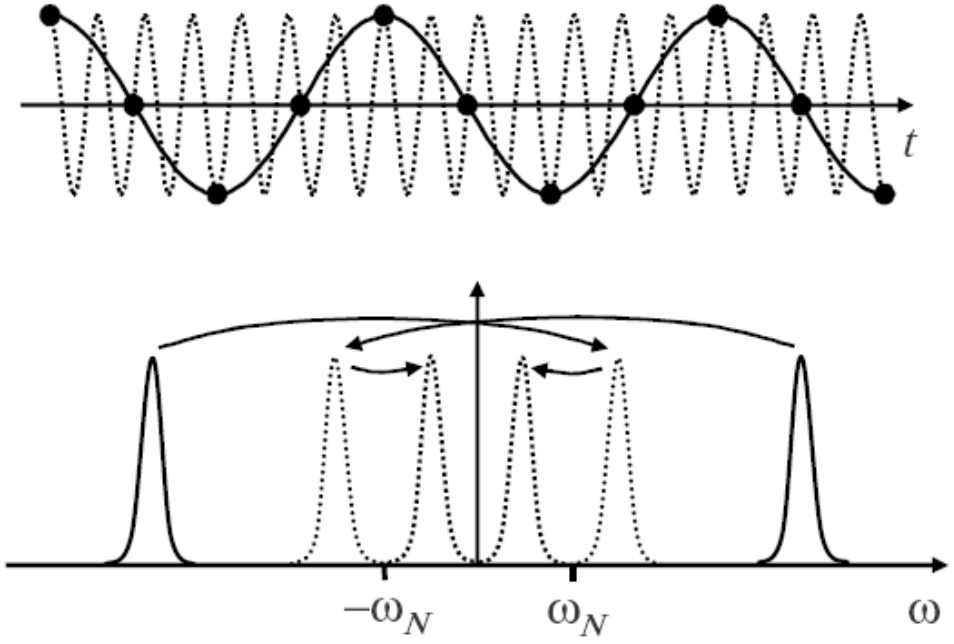

Figure 3.9: Example of Undersampling: sine wave with $\omega = 3.5\omega_N$ (dotted line) that appears as $\omega = 0.5\omega_N$ (solid line) due to the long time steps (dots). Below the consequent *folding* of the spectra.

are collected, then frequencies higher than the Nyquist frequency will be *aliased* (see Fig. 3.9), and the individual frequency-shifted copies of the original transform are called *aliases*. This procedure creates many copies of the original signal, whose frequency offset is the sampling frequency, ω_S.

The condition for a non-destructive sampling rate is that the aliases of both adjacent bands do not overlap when shifted by all integer multiples of ω_S. Now if the frequency range in which the signal falls is known then it is straightforward to convert the aliased spectrum at frequency ω into the proper frequency ω_0 using the relationship [28]:

$$\omega_0 = (-1)^m \omega + m \cdot \omega_N \tag{3.4}$$

where m is an integer equal to the number of times the signal has been undersampled. In this way it is possible to collect a significantly less dense number of points in the time domain, and hence drastically reduce scanning speed and in turn acquisition times.

Conclusion and perspective

The ensemble of Coherent Raman Techniques can provide a large quantity of information with high specificity and sensitivity. Single colour techniques (CARS, SRS and RIKE) have been widely developed but, in order to achieve better results and ideally single shot measurement of all Raman spectra, broadband sources are needed. In this work some interesting features of the broadband techniques have been demonstrated. Of course, large improvements has to be done in order to make this new approaches competitive.

CARS is the simplest technique in terms of set-up and implementation(in particular the detection chain), the major problem is the distortion of detected signal provided by the Non-resonant Background. Several configuration(as shown in Chapter 1) can be implemented to cancel out this spurious contribution. In the particular case of broadband CARS, applying a certain delay between the pump and Stokes pulses (in order to make them only partially overlapped) is possible to retrieve enough clean spectra to recognize the characteristic signatures of the examined species, reducing significantly the Non-resonant background. Hence to improvements on CARS set-up must head in this is the direction.

In this work an original method to recover the broadband SRS spectrum by using FT spectroscopy was introduced. The method exploits the ultrastable and reproducible positioning of the TWINS interferometer, the balanced detection and lock-in amplification with high frequency modulation. We have shown that we can easily recover broadband SRS spectra of different solvents, and that we could perform imaging and distinguish PMMA and PS based on their full spectra. Being this method completely new, large improvements

have to be done. In fact, SRS microscopy is currently at a stage where it is possible to obtain images at video rate of biological samples by probing at a single frequency. Our imaging system, on the other hand, still requires very long acquisition time but future use of methods as the *undersampling* will allow to gain more than 2 orders of magnitude in speed, while fast scanning of the sample will allow to use higher pump power and gain up to another order of magnitude. It is worth remembering that the spectral resolution is not affected by the sampling rate but only by the scan length in time domain (and of course from the spectral width of the pump), so this undersampling procedure would not affect our resolution.

The developed approach is original in the sense that we rapidly measure the full spectra covered by the Stokes pulse at each pixel. This translates in a long imaging time, as we have at the moment a pixel dwell time of the order of 1s. There is a win-win factor when considering the pump power that can be sent to the sample. Indeed, sample damage currently limits the pump power used in the experiment. Translating the sample at higher speed would make it possible to use higher pump intensities without damage, which would turn in a higher SNR, thus allowing one to acquire the same amount of signal in less time. In our case though, the time to scan the full wedges size cannot be made much faster, even if the use of more conventional Michelson interferometer with delay tracking would allow to gain speed in this regard. The strategy we would like to follow consists in staying at a position of the interferometer during a full 2D scan of the sample, and then move to a new wedge position until we have enough images at different delays to reconstruct the time-domain interferogram for each pixel. In this way, we expect to reduce the number of temporal delays to be acquired using the TWINS from the actual 40000 to approximately 100, thus significantly increasing the measurement speed. This is precisely one of the great advantages of the wedge interferometer, which remains phase locked to a very high accuracy if we do not move it, and has a very reproducible positioning. We can estimate that if we neglect for now the positioning delay, undersampling will permit to acquire images 400 times faster, without considering the fact that we will be able to increase pump power at the sample.

To summarize we have seen that this approach could be a starting point for future developments. The potentiality of this method are promising even though now many limiting factors are present. Indeed, when it will be possible to scan faster, this method could be applied to biological samples.

Appendix A

Birefringence

In this Appendix I will go through the key part of the Broadband SRS (see Chapter 3) setup, the TWINS (Translating-Wedge-Based Identical Pulses eNcoding System) interferometer which is a simple and compact optical device which exploits birefringence generate two delayed, phase-locked collinear replicas of an input pulse.

A.1 Birefringence

To fully understand the behavior of the TWINS it is necessary to describe the *birefringence*, an optical property of some materials having a refractive index that depends on the polarization and propagation direction of light[30]. These optically anisotropic materials are said to be *birefringent* (or *birefractive*). The birefringence is often quantified as the maximum difference between refractive indices exhibited by the material. Crystals with asymmetric crystal structures are often birefringent, as well as plastics under mechanical stress. Birefringence is responsible for the phenomenon of double refraction whereby a ray of light, when incident upon a birefringent material, is split by polarization into two rays taking slightly different paths. This optical property is caused by the anisotropy of the electrical permittivity ε.

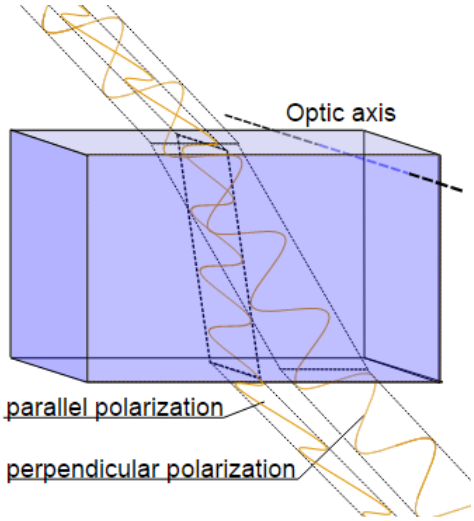

Figure A.1: Incoming light in the parallel (s) polarization sees a different effective index of refraction than light in the perpendicular (p) polarization, and is thus refracted at a different angle.

Uniaxial material

The simplest (and most common) type of birefringence is described as uniaxial, meaning that there is a single direction governing the optical anisotropy whereas all directions perpendicular to it (or at a given angle to it) are optically equivalent. Thus rotating the material around this axis does not change its optical behavior. This special direction is known as the optic axis of the material.

Light whose polarization is perpendicular to the optic axis(thus propagating along optical axis) is governed by a refractive index n_o (for "ordinary"). Light whose polarization is in the direction of the optic axis sees an optical index n_e (for "extraordinary"). For any ray direction there will be a polarization direction perpendicular to the optic axis, and this is called an ordinary ray. However for most ray directions the other polarization direction will be partly in the direction of the optic axis, and this is called an extraordinary ray. The ordinary ray will always experience a refractive index of n_o, whereas the refractive index of the extraordinary ray will be in between n_o and n_e,

depending on the ray direction. The magnitude of the difference is quantified by the **birefringence**:

$$\Delta n = n_e - n_o \tag{A.1}$$

The propagation of the ordinary ray is simply described by n_o as if there were no birefringence involved. However the extraordinary ray, as its name suggests, propagates unlike any wave in a homogeneous optical material. Its refraction (and reflection) at a surface can be understood using the effective refractive index (a value in between n_o and n_e).

When an arbitrary beam of light strikes the surface of a birefringent material, the polarizations corresponding to the ordinary and extraordinary rays generally take different paths. Unpolarized light consists of equal amounts of energy in any two orthogonal polarizations, and even polarized light (except in special cases) will have some energy in each of these polarizations. According to Snell's law of refraction, the angle of refraction will be governed by the effective refractive index which is different between these two polarizations. The different angles of refraction for the two polarization components are shown in the Fig. A.1, with the optic axis along the surface (and perpendicular to the plane of incidence), so that the angle of refraction is different for the p polarization (the "ordinary ray" in this case, having its polarization perpendicular to the optic axis) and the s polarization (the "extraordinary ray" with a polarization component along the optic axis).

In a birefringent material, a wave consists of two polarization components which generally are governed by different effective refractive indices. The so-called *slow ray* is the component for which the material has the higher effective refractive index (slower phase velocity), while the *fast ray* is the one with a lower effective refractive index. When a beam is incident on such a material from air (or any material with a lower refractive index), the slow ray is thus refracted more towards the normal than the fast ray. In the Fig. A.1, it can be seen that refracted ray with s polarization in the direction of the optic axis (thus the extraordinary ray) is the slow ray in this case.

Uniaxial birefringence is classified as *positive* when the extraordinary

Table A.1: Characteristics of a selection of birefringent materials. GVM: group velocity mismatch between ordinary and extraordinary polarizations(citare julien e co).

Material	Ord. index	Birefr. ($n_e - n_o$)	Range (μm)
$LiNbO_3$	2.1142	-0,0583	0.4-5.2
Hg_2Cl_2	1.8976	0.549	0.4-20
LiO_3	1.8163	-0.109	0.5-5
Tl_4HgI_6	2.3914	0.0688	1.0-60
Tl_3AsSe_3	3.3651	-0.187	2-12
α-BaB_2O_4	1.6579	-0.12	0.19-3.5

index of refraction ne is greater than the ordinary index n_0. *Negative* birefringence means that $\Delta n = n_e - n_o$ is less than zero. In other words, the polarization of the fast (or slow) wave is perpendicular to the optic axis when the birefringence of the crystal is positive (or negative, respectively).

For the sake of completeness it is important to mention also the case of *biaxial crystals* which is substantially more complex because they are characterized by three refractive indices corresponding to two principal axes of the crystal.

Birefringent materials

The best-characterized birefringent materials are crystals. Due to their specific crystal structures their refractive indices are well defined. Depending on the symmetry of a crystal structure (as determined by one of the 219 possible crystallographic space groups), crystals in that group may be forced to be anisotropic (non-birefringent), to have uniaxial symmetry or not, in which case it is a biaxial crystal. In Tab. A.1 some examples of birefringent materials are shown.

A.1.1 Theory

Birefringence results when a material's permittivity is not describable using a scalar value, but requires a tensor to relate the electric displacement ($\mathbf{D}$) with

the electric field (**E**). Consider a plane wave propagating in an anisotropic medium, with a permittivity tensor ε_{ij}, with i, j=1,2,3, and assuming no magnetic permeability in the medium:$\mu = \mu_0$.

We shall assume that the electric field of a wave of angular frequency ω can be written in the form:

$$\mathbf{E} = \mathbf{E}_0 \exp[i(\omega t - \mathbf{k} \cdot \mathbf{r})] \tag{A.2}$$

where $\mathbf{r}$ is the position vector, t is time, and $\mathbf{E}_0$ is a vector describing the electric field at $\mathbf{r} = 0$,$t = 0$. Then we shall find the possible wave vectors $\mathbf{k}$ using Maxwell's equations from which we obtain(see Eq. 1.12):

$$\nabla \times \nabla \times \mathbf{E} = -\mu_0 \frac{\partial^2 \mathbf{D}}{\partial t^2} \tag{A.3a}$$

$$\nabla \cdot \mathbf{D} = 0 \tag{A.3b}$$

where the electric displacement vector $\mathbf{D}$ is related to the electric field $\mathbf{E}$ through the permittivity tensor ε_{ij}:

$$\mathbf{D} = \varepsilon_{ij} \mathbf{E} \tag{A.4}$$

Substituting the definition of $\mathbf{D}$ and Eq. A.2 into Eq. A.3(a-b) leads to the conditions:

$$|\mathbf{k}|^2 \mathbf{E}_0 - (\mathbf{k} \cdot \mathbf{E}_0)\mathbf{k} = \mu_0 \omega^2 (\varepsilon_{ij} \mathbf{E}_0) \tag{A.5a}$$

$$\mathbf{k} \cdot (\varepsilon_{ij} \mathbf{E}_0) = 0 \tag{A.5b}$$

Eq. A.5b indicates that $\mathbf{D}$ is orthogonal to the direction of the wavevector $\mathbf{k}$. To find the allowed values of $\mathbf{k}$, $\mathbf{E}_0$ can be eliminated from Eq. A.5a. If Eq. A.5a is written in Cartesian coordinates with the x, y and z axes chosen in the principal directions of the permittivity tensor ε, then:

$$\varepsilon = \varepsilon_0 \begin{bmatrix} n_x^2 & 0 & 0 \\ 0 & n_y^2 & 0 \\ 0 & 0 & n_z^2 \end{bmatrix} \tag{A.6}$$

where the diagonal values are squares of the refractive indices for polarizations along the three principal axes x, y and z. With ε in this form, and noting that the speed of light $c = 1/\sqrt{\mu_0 \varepsilon_0}$ Eq. A.5a becomes:

$$(-k_y^2 - k_z^2 + \frac{\omega^2 n_x^2}{c^2})E_x + k_x k_y E_y + k_x k_z E_z = 0 \tag{A.7a}$$

$$k_x k_y E_x + (-k_x^2 - k_z^2 + \frac{\omega^2 n_y^2}{c^2})E_y + k_y k_z E_z = 0 \tag{A.7b}$$

$$k_x k_z E_x + k_y k_z E_y + (-k_x^2 - k_y^2 + \frac{\omega^2 n_z^2}{c^2})E_z = 0 \tag{A.7c}$$

where E_x , E_y, E_z and k_x, k_y, k_z are the components of $\mathbf{E}_0$ and $\mathbf{k}$. This is a set of linear equations in E_x , E_y, E_z and they have a non-trivial solution if the following determinant is zero:

$$\begin{vmatrix} (-k_y^2 - k_z^2 + \frac{\omega^2 n_x^2}{c^2})E_x & k_x k_y & k_x k_z \\ k_x k_y & (-k_x^2 - k_z^2 + \frac{\omega^2 n_y^2}{c^2}) & k_y k_z \\ k_x k_z & k_y k_z & (-k_x^2 - k_y^2 + \frac{\omega^2 n_z^2}{c^2}) \end{vmatrix} = 0 \tag{A.8}$$

Evaluating the determinant of Eq. A.8, and rearranging the terms, we obtain:

$$\begin{aligned} \frac{\omega^4}{c^4} - \frac{\omega^2}{c^2}(\frac{k_x^2 + k_y^2}{n_z^2} + \frac{k_x^2 + k_z^2}{n_y^2} + + \frac{k_y^2 + k_z^2}{n_x^2}) + \\ (\frac{k_x^2}{n_y^2 n_z^2} + \frac{k_y^2}{n_x^2 n_z^2} + \frac{k_z^2}{n_x^2 n_y^2})(k_x^2 + k_y^2 + k_z^2) = 0 \end{aligned} \tag{A.9}$$

In the case of a uniaxial material, choosing the optic axis to be in the z direction so that$n_x = n_y = n_o$ and $n_z = n_e$, this expression can be factored into

$$(\frac{k_x^2}{n_o^2}+\frac{k_y^2}{n_o^2}+\frac{k_z^2}{n_o^2}-\frac{\omega^2}{c^2})(\frac{k_x^2}{n_e^2}+\frac{k_y^2}{n_e^2}+\frac{k_z^2}{n_o^2}-\frac{\omega^2}{c^2})=0 \tag{A.10}$$

Setting either of the factors in Eq. A.10 to zero will define an ellipsoidal surface in space of allowed wave vectors **k**. The first factor being zero defines a sphere corresponding to ordinary rays, in which the effective refractive index is exactly n_o. The second defines a spheroid symmetric about the z axis. This solution corresponds to extraordinary rays in which the effective refractive index is in between n_o and n_e. Therefore for any arbitrary direction of propagation, two distinct wavevectors **k** are allowed corresponding to the polarizations of the ordinary and extraordinary rays. A general state of polarization launched into the medium can be decomposed into two such waves which will then propagate with different k vectors (except in the case of propagation in the direction of the optic axis).

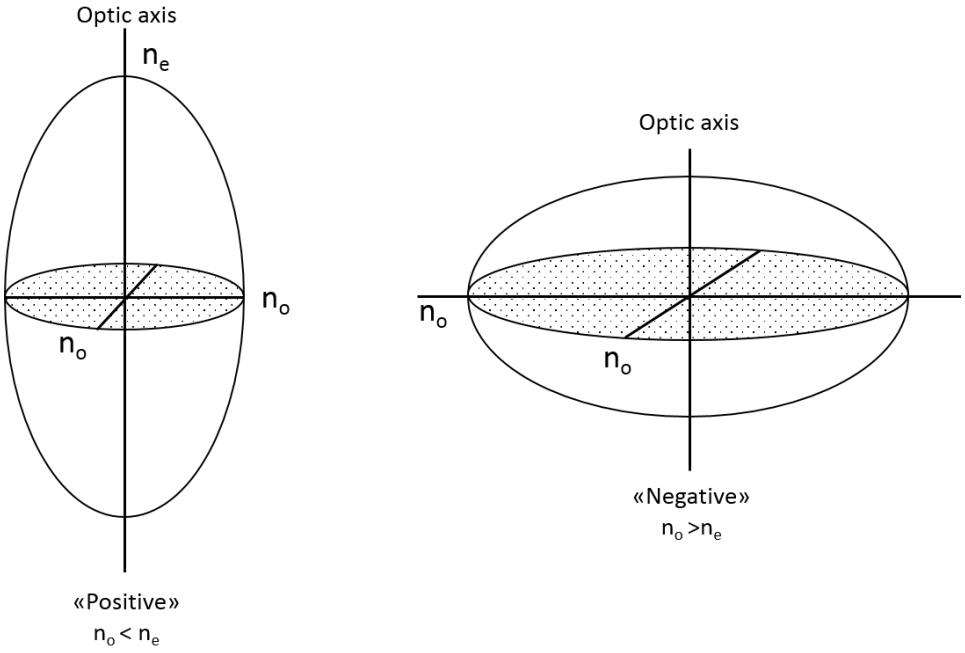

Figure A.2: Ellipsoid of refractive index for positive and negative birefringence.

Bibliography

[1] C. H. Camp Jr, Y. J. Lee1, J. M. Heddleston, C. M. Hartshorn, A. R. Hight Walker, J. N. Rich, J. D. Lathia, and M. T. Cicerone, "High-speed coherent Raman fingerprint imaging of biological tissues," *Nature Photonics*, p. 627–634, July 2014.

[2] A. Weiner, *Ultrafast Optics*. John Wiley and Sons, 2011.

[3] M. D. Levenson and S. K. Satoru, *Introduction To Nonlinear Laser Spectroscopy*. Academic Press, 1988.

[4] M. Wei, C. W. Freudiger, L. Sijia, and X. S. Xie, "Coherent Nonlinear Optical Imaging: Beyond Fluorescence Microscopy," *Annu. Rev. Anal. Chem.*, vol. 62, p. 507–530, July 2011.

[5] E. O. Potma, C. L. Evans, and X. S. Xie, "Heterodyne coherent anti-stokes raman scattering (cars) imaging," *OPTICS LETTERS*, vol. 31, January 2006.

[6] F. Ganikhanov, C. L. Evans, B. G. Saar, and X. S. Xie, "High-sensitivity vibrational imaging with frequency modulation coherent anti-stokes raman scattering (fm cars) microscopy," *OPTICS LETTERS*, vol. 31, June 2006.

[7] A. Volkmer, L. D. Book, and X. S. Xie, "Time-resolved coherent anti-stokes raman scattering microscopy: Imaging based on raman free induction decay," *APPLIED PHYSICS LETTERS*, vol. 80, March 2002.

[8] J.-X. Cheng, L. D. Book, and X. S. Xie, "Polarization coherent anti-stokes raman scattering microscopy," *OPTICS LETTERS*, vol. 26, September 2001.

[9] M. Levenson, *Introduction to Nonlinear Laser Spectroscopy-Elsevier Science*. Academic Press, Inc,, 1988.

[10] C. W. Freudiger, M. B. J. Roeffaers, X. Zhang, B. G. Saar, W. Min, and X. S. Xie, "Optical Heterodyne-Detected Raman-Induced Kerr Effect (OHD-RIKE) Microscopy," *J. Phys. Chem. B*, vol. 18, p. 5574–5581, April 2011.

[11] F. Adler, A. Sell, F. Sotier, R. Huber, and A. Leitenstorfer, "Attosecond relative timing jitter and 13fs tunable pulses from a two-branch er:fiber laser," *Optics Letters*, vol. 32, no. 3504, 2007.

[12] F. Tauser, F. Adler, and A. Leitenstorfer, "Widely tunable sub-30-fs pulses from a compact erbium-doped fiber source," *Optics Letters*, vol. 29, no. 516, 2004.

[13] Y. Liu, Y. Jong Lee, and M. T. Cicerone*, "Broadband cars spectral phase retrieval using a time-domain kramers–kronig transform," *Optics Letters*, vol. 34, May 2009.

[14] L. Kong, M. Ji, G. R. Holtom, D. Fu, C. W. Freudiger, and X. S. Xie, "Multicolor stimulated raman scattering microscopy with a rapidly tunable optical parametric oscillator," *Optics Letters*, vol. 38, January 2013.

[15] Y. Ozeki, W. Umemura, Y. Otsuka, S. Satoh, H. Hashimoto, K. Sumimura, N. Nishizawa, K. Fukui, and K. Itoh, "High-speed molecular spectral imaging of tissue with stimulated raman scattering," *Nature Photonics*, vol. 6, November 2012.

[16] A. Lau, W. Werncke, K. Pfeiffer, M.and Lenz, and H. J. Weigmann, "Inverse raman scattering," *Sov. J. Quant. Electron.*, vol. 6, April 1976.

[17] K. Seto, Y. Okuda, E. Tokunaga, and T. Kobayashi, "Development of a multiplex stimulated raman microscope for spectral imaging through multi-channel lock-in detection," *Rev. Sci. Instrum.*, vol. 84, no. 4, 2013.

[18] E. Ploetz, S. Laimgruber, S. Berner, W. Zinth, and P. Gilch, "Femtosecond stimulated raman microscopy," *Applied Physics B*, vol. 87, May 2008.

[19] P. Griffiths and J. de Hasseth, *Fourier Transform Infrared Spectroscopy*. Wiley-Blackwell, 2007.

[20] D. Brida, C. Manzoni, and G. Cerullo, "Phase-locked pulses for two-dimensional spectroscopy by a birefringent delay line," *OPTICS LETTERS*, vol. 37, August 2012.

[21] J. Rèhault, M. Maiuri, C. Manzoni, D. Brida, J. Helbing, and G. Cerullo, "2D IR spectroscopy with phase-locked pulse pairs from a birefringent delay line," *OPTICS EXPRESS*, vol. 22, April 2014.

[22] J. Rèhault, M. Maiuri, A. Oriana, and G. Cerullo, "Two-dimensional electronic spectroscopy with birefringent wedges," *AIP*, vol. 85, no. 8, 2014.

[23] G. Ghosh, "Sellmeier Coefficients and Dispersion of Thermo-Optic coefficients for some optical glasses," *Applied Optics*, vol. 85, April 1997.

[24] W. Persson and S. Svanberg, *Laser Spectroscopy VIII*. Springer, 1987.

[25] J. Jaumot, A. de Juanb, and R. Tauler, "Mcr-als gui 2.0: New features and applications," *Chemometrics and Intelligent Laboratory Systems*, vol. 140, November 2014.

[26] S. Aloïse, C. Ruckebusch, L. Blanchet, J. Réhault, G. Buntinx, and J.-P. Huvenne, "The benzophenone states intersystem crossing reinvestigated by ultrafast absorption spectroscopy and multivariate curve resolution," *J. Phys. Chem. A*, vol. 87, no. 2, 2008.

[27] T. Hirschfeld, "Fellgett's advantage in uv-vis multiplex spectroscopy," *Applied Spectroscopy*, vol. 30, no. 1, 1976.

[28] P. Hamm and M. Zanni, *Concepts and Methods of.*

[29] B. G. Saar, C. W. Freudiger, J. Reichman, C. M. Stanley, G. R. Holtom, and X. S. Xie, "Video-rate molecular imaging in vivo with stimulated raman scattering," *Science*, vol. 330, December 2010.

[30] M. Born and E. Wolf, *Principles of Optics.* 1999.

[31] O. Svelto, *Principles of Lasers, FOURTH EDITION.* Springer, 2010.

[32] L. E. Conor and X. S. Xie, "Coherent Anti-Stokes Raman Scattering Microscopy: Chemical Imaging for Biology and Medicine," *Annu. Rev. Anal. Chem.*, vol. 19, p. 883–909, Aug 2008.

[33] R. Selm, M. Winterhalder, A. Zumbusch, G. Krauss, T. Hanke, A. Sell, and A. Leitenstorfer, "Ultrabroadband background-free coherent anti-stokes raman scattering microscopy based on a compact er:fiber laser system," *OPTICS LETTERS*, vol. 35, October 2010.